eTransportation 24 (2025) 100410

Contents lists available at ScienceDirect

eTransportation

journal homepage: www.journals.elsevier.com/etransportation

Degradation of lithium-ion batteries under automotive-like conditions: P2D model-based understanding and ex-situ validation

G. Sordi [a,b,c], A. Stecchini [a], R. Evangelista [a], D. Luder [b,c], W. Li [b,c], D.U. Sauer [b,c,d], A. Casalegno [a], C. Rabissi [a,*]

[a] Politecnico di Milano, Department of Energy, via Lambruschini 4, 20156, Milano, Italy
[b] Chair for Electrochemical Energy Conversion and Storage Systems, Institute for Power Electronics and Electrical Drives (ISEA), RWTH Aachen University, 52074, Aachen, Germany
[c] Center for Ageing, Reliability and Lifetime Prediction of Electrochemical and Power Electronic Systems (CARL), RWTH Aachen University, 52074, Aachen, Germany
[d] Helmholtz Institute Münster (HI MS), Forschungszentrum Jülich, Jülich, Germany

ARTICLE INFO

Keywords:
Lithium-ion batteries
Degradation
Diagnostics
Driving cycle
Model

ABSTRACT

Despite its worldwide commercialisation, the degradation of lithium-ion battery technology is still a hot research topic. Batteries are known to decrease in capacity and increase in internal resistance, but it is quite uncommon to further investigate the performance decay, distinguishing classes of ageing mechanisms (resistive, kinetic and mass-transport) and relating them with the operation. This work exploits the P2D model to understand the performance decay of ageing cells from a physical perspective. A complex experimental campaign combining 13 different automotive-like cycles, applied to commercial battery samples to recreate the degradation of batteries under realistic conditions, is analysed with such methodology. Along the ageing tests, physical models' parameters are periodically identified by means of particle swarm optimisation applied over characterisation tests. Parameter evolution is then correlated with specific degradation mechanisms, related operating conditions and performance decay. A significant decrease in electrolyte conductivity and lithium solid-state diffusivity within the positive electrode are detected, progressively inducing heterogeneous operation and worsening of both efficiency and capacity retention. Particularly, cycle depth appears to promote particle cracking and loss of positive electrode material. Post-mortem analyses are then performed to support the interpretations on degradation mechanisms, confirming the degradation of electrolyte and positive electrode.

1. Introduction

Lithium-ion battery (LIB) is widely considered a key technology for the decarbonisation of the transportation sector. However, a LIB is known to age both over storage and operational time and, depending on its utilization, to show a worsening in performance under different perspectives, such as capacity reduction and resistance rise [1,2]. Battery degradation is a significant aspect to consider to evaluate the economic and environmental feasibility of electric vehicles. Nevertheless, the relation between the operating conditions and the effect on the performance and lifetime is not fully consolidated in the scientific literature due to the large variety of possible mechanisms taking place at the same time, with the interplay among them leading to hardly distinguishable effects on the performance [1,2]. As brilliantly summarised in Ref. [1], degradation mechanisms can be classified as 5 main mechanisms and 13 secondary mechanisms, all inducing 5 ageing modes, observable at cell scale. These mechanisms superimpose and combine with each other, causing mixed performance worsening effects, manifest in the form of capacity and power loss. In Ref. [3], a dedicated review to the automotive application is provided, collecting results from many scientific articles regarding common chemistries, driving and charging schedules and the impact of different stressors on degradation. This work provides valuable guidelines to prolong battery lifetime.

Many works in the literature investigate degradation under various conditions [4–7], primarily concentrating on capacity loss and increased internal resistances. For instance, in Ref. [4] a wide experimental campaign was conducted to investigate degradation under different conditions. The authors succeeded in gathering interesting insights on the role of the operating conditions, providing formulas to estimate capacity loss depending on temperature, time, charge throughput and

* Corresponding author.
E-mail address: claudio.rabissi@polimi.it (C. Rabissi).

https://doi.org/10.1016/j.etran.2025.100410
Received 30 June 2024; Received in revised form 21 November 2024; Accepted 26 February 2025
Available online 28 February 2025
2590-1168/© 2025 The Authors. Published by Elsevier B.V. This is an open access article under the CC BY license (http://creativecommons.org/licenses/by/4.0/).

applied current. However, they could provide only limited explanations to the origin of losses. The use of low C-rate discharge as diagnostic tool enabled to identify some thermodynamic trends, but regarding kinetics and mass-transport limitations the insights were limited, related to the trend of power decay. While these metrics are crucial indicators, they alone are insufficient for accurately assessing battery health and comprehending cell performance across diverse operational scenarios. Furthermore, these investigations frequently employ constant-current cycles, which fail to mimic real-world dynamic usage patterns. Jalkanen et al. [8] investigated three different operating conditions, but with a more comprehensive approach, including capacity loss, electrochemical impedance spectroscopy and a wide post-mortem analysis. This solution is definitely interesting in a laboratory for deep investigations, but it is not feasible to investigate many operating conditions, with different types of specific equipment and relying on end-of-life and invasive measurements.

Physical models can be a suitable tool to reproduce the behaviour of aged cells, saving on experimental time and avoiding destructive measurements [7,9–11]. Since they include a proper description of the complex phenomena occurring with the operation of a LIB cell, a satisfactory capability of reproducing the experimental data can be achieved. One possibility is by modelling aging mechanisms explicitly. For instance, Luo et al. [7] implemented the equations to describe solid electrolyte interphase (SEI) layer growth, lithium plating, particle cracking, and loss of active material (LAM) in the pseudo-two-dimensional (P2D) model. They provided great insights into the role of the operating conditions (e.g. state of charge swing) on degradation and on their mutual interplay. However, the only target for their simulation was the capacity decay trend and the cycling experiment included only constant-current cycles.

Another possibility is the usage of a performance model, without an explicit description of degradation mechanisms. In this framework, by comparing the values of relevant physical parameters between fresh and aged states, it is possible to identify the most likely class of phenomena inducing these effects and estimate the pace of their evolution. For instance, L. Zhang et al. [11] proposed to trace the evolution of parameters of a P2D model with a thermal model along the battery lifetime as a diagnostic tool. They applied the method by investigating nine key parameters to identify the sources of overpotentials and link them to the occurrence of SEI growth. They succeeded in providing a more comprehensive description of the battery state of health, though the evolution of some parameters was not linked to distinct degradation mechanisms and the operating conditions (constant-current cycling at 50 °C) are not representative of a real-life usage. K. Uddin et al. [9] followed the same approach with a P2D model and they applied it to a calendar-aged cell. However, they reduced the number of fitting parameters to three, consistently with the expected degradation phenomena as a demonstration, without exploiting it for diagnostic purposes. Analogously, Kim et al. [12] identify effective parameters within the P2D model that are suitable for accurate battery degradation diagnosis. The study utilizes a genetic algorithm for the parameters identification process and determines their confidence intervals, adopting multiple operation profiles to prevent overfitting during the identification process. Several Li-ion batteries are tested, demonstrating high confidence in P2D model parameters identification: solid diffusion coefficients, reaction rate constants, and stoichiometry limits exhibit clear trends as the battery ages, making them valuable indicators for diagnosing battery degradation. Despite the effectiveness of this study, it does not aim to a comprehensive analysis, lacking an experimental campaign with various aging cycles and of detailed discussion of aging mechanisms and their correlation with physical parameters. Also, the work [13] focuses on analysing the decay of parameters within the P2D model to gain insights into lithium-ion battery degradation mechanisms. A novel approach is proposed, utilizing the incremental capacity curve as a fitting target alongside the discharge curve and incremental capacity analysis (ICA) curve, as a direct indicator of battery aging. The researchers employ two algorithms, a non-dominated sorting genetic algorithm and a deep neural network, to identify model parameters. Interestingly, strong correlations are observed between battery state of health and specific parameters, such as the initial lithium-ion concentration in the negative electrode, but their significance as indicators of specific aging mechanisms is not discussed.

Similar scope with a different modelling approach is proposed in the work by Lyu et al. [14], where a simplified electrochemical model (EM) is adopted for monitoring internal degradation in lithium-ion batteries. The authors develop this EM by reorganizing the parameters of the single particle model (SP) for easier identification and attributing a specific physical meaning to each parameter. Model parameter identification is performed using a combined load profile for improved accuracy and validated with cyclic aging experiments under various conditions (25 °C/1C, 25 °C/2C, 50 °C/1C, and 50 °C/2C). The identified parameters, including internal resistance and parameters related to solid-phase diffusion, double-layer capacitance, and reaction kinetics, exhibit strong correlations with experimentally observed capacity fading. The method reduces the gap between EMs and in situ investigation of battery degradation, providing interesting insights into battery performance loss, but the work does not stress the identifiability of specific battery aging mechanisms and the representativity of real-life operating conditions is overlooked. Also in Ref. [15], the authors present a method for the quantitative analysis of battery aging modes by identifying changes in physical parameters using an improved Single Particle model. They investigate correlation of aging modes at various conditions by tracking changes in physical parameters such as loss of lithium inventory (LLI), effective porosity of electrodes, particle radius, diffusion coefficient and reaction rate constants. While the study finds interesting correlations between SOH and specific physical parameters evolution, such as LLI and electrolyte diffusion coefficient, the study focuses on very specific operating conditions, aging batteries at constant rates of 1C and 2C, falling short in terms of representativeness of real-life application. Concluding, the study [16] investigates non-destructive diagnostics and quantifies battery aging under various degradation paths. The researchers employ a reduced-order electrochemical-spatial-phase-model (ESPM) to identify aging-related parameters in commercial NCA||C 18650 lithium-ion cells. Experimental data from four groups of cells, subjected to different cycling and calendar aging conditions, are used in this study. The ESPM demonstrates its effectiveness in predicting battery discharge voltage along the aging. The analysis of identified parameters reveals distinct trends in thermodynamic, mass transport, and kinetic parameters across the different aging conditions, highlighting the model's capability to capture various degradation mechanisms. While very wide, including differentiation between cycle and calendar aging effects and to quantify cell-to-cell variations in degradation, the study does not provide any specific conclusion regarding automotive related aging in real-life conditions nor validates the interpretation with post-mortem analyses.

In order to exploit physical parameter estimation as a diagnostic tool, the selection of the parameters to be identified should not bias the solution in any direction, the solution must be unique and the reliability of the model must be verified. Moreover, the ideal method should not rely on time-consuming measurements to speed up the procedure. Summarizing, to the authors knowledge, no work in the literature comprehensively focuses on identifying and understanding from a physical perspective the specific degradation mechanisms involved with automotive-like operation as a function of different operating conditions, nor aims at validating the findings with post-mortem analyses. Demonstrating the P2D model to be able to progressively quantify a set of key physical parameters by reproducing experimental diagnostic tests would consolidate the understanding of performance decay.

Hence, in this work, we exploit physical models to elucidate on degradation phenomena in lithium-ion cells under automotive-like conditions, specifically focusing on the effect of operational parameters. We perform 13 types of aging cycles on commercial cells and collect

data from periodic check-ups. Based on these data and an optimisation algorithm, the P2D model parameters are identified for fresh and increasingly aged states. In this way, we are able to draw the evolution of physical parameters over time and cycles for different combinations of operating conditions. The P2D model provides a comprehensive simulation of battery operation, resulting in reliability, and the parameters trend enables the physical interpretation of ageing, namely the identification of the most likely degradation mechanisms ongoing in the cells and their relation with the operating conditions that promote them. Moreover, in the end, we attempt to verify the reliability of the interpretations with post-mortem investigations, closing the loop and strengthening the suitability of this methodology. The use of an optimised sequence of tests shortens testing time, while the exploitation of an optimisation algorithm aims at an objective and repeatable solution. This work deepens the results collected in Ref. [17] to widen the understanding of the effects on the performance of each operating condition. Since the cycle conditions are selected to reproduce close-to-real-world conditions that a battery experiences on a fully electric vehicle, this work provides useful insights regarding realistic degradation, making a step ahead towards real usage with respect to other works with similar approaches [18,19], still resulting effective as an investigation tool suitable for advanced diagnostic and scientific environments.

This publication is organised as follows. First, the experimental and modelling tools are summarised in Section 2. Section 3 is dedicated to the results, and Section 4 reports a set of validation measurements to verify the reliability of the model-based interpretation of ageing. Due to the large amount of data, Section 3 focuses on one operating condition to identify general trends, and then it details the effect of the operating conditions. Finally, Section 4 reports on the results of the post-mortem analyses, comparing the interpretations derived from the modelling analyses with evidence of degradation from either a chemical composition, morphological or capacity retention point of view.

2. Methodology

An overview of the methodology is reported here, while the details are provided in the following paragraphs.

- On commercial battery samples (see Section 2.1), an articulated driving cycle aging campaign (see Section 2.2) is carried out under different operating conditions. Characterisation tests (see Section 2.3) are performed periodically to evaluate the residual performances.
- The most important physical parameters of the P2D model are quantified exploiting an optimisation algorithm (see Section 2.4) aiming at reproducing the characterisation tests with the model. This procedure is periodically repeated along the driving cycle campaign for several degradation states, enabling the visualisation of the variation trends of the parameters.
- These trends are investigated to identify possible correlations among parameters and propose a physical interpretation of degradation, suggesting the most likely responsible degradation phenomena.
- At the end of the campaign, a selected set of samples is disassembled in an inert environment. The reliability of the interpretation of degradation phenomena is then verified against post-mortem analyses.

A detailed description of experimental activities and modelling tools is provided in the following sections. For any further information regarding the methodology, the reader is referred to Ref. [19].

2.1. Experimental sample and testbench

The experimental samples are commercial Li-ion battery cells with a blended positive electrode of lithium-nickel-cobalt-manganese-oxide (NMC), lithium-manganese oxide (LMO), and graphitic negative electrode. Cells are cylindrical 18650 type with 2.25 Ah of nominal capacity. A summary of technical information is reported in Table 1.

As samples were acquired in different batches during the activity, actual as-received performances were evaluated for each sample of interest at the beginning of the campaign. These data are later referred to as begin-of-life (BOL) performances.

The testing station is custom-developed. It includes one power supply (NI RMX-4124) and two five-channel electronic loads (Chroma UM 63640-80-80), resulting in eight independent testing channels with impedance measurement, capable of 80 A maximum current each. A Binder MKF 720 Eucar 6 climatic chamber hosts the samples during both cycling and characterisation periods at known and controllable environmental temperatures (in the range −40 °C/+120 °C). Cells' temperature is monitored through thermocouples attached to their surface and acquired by means of dedicated acquisition board (NI 9201). For additional information, the reader is referred to Ref. [19].

2.2. Test matrix

Three different load profiles are selected and applied in order to span a reasonably wide and consistent range of combinations beneath average C-rate and dynamicity of operation: the Worldwide harmonised Light vehicles Test Procedure (referred to as WLTP), its modified version "WLTP High-Speed" and the standard of the International Electrotechnical Commission (IEC) 62660–1 [21] (here referred to as IEC for brevity). WLTP is characterised by relatively low C-rates, with frequent regenerative braking events. WLTP High-Speed includes only the third and fourth sections of the WLTP (corresponding to highway driving), resulting in less regenerative events and higher average discharge C-rate with respect to the standard WLTP profile. IEC, finally, is a stepped profile designed to test the durability of batteries for battery electric vehicles, with relatively higher discharge and charge C-rate with respect to WLTP. For additional information regarding the load profiles, the reader is referred to Ref. [17].

The three load profiles have been investigated under different conditions of environmental temperature, state of charge (SoC) window and charge C-rate, overall resulting in 13 different combinations of operational conditions, whose literature-based selection has been discussed in Ref. [17] and are hereby listed in Table 2 (where EFC indicates Equivalent Full Cycles, pointing out the duration of the aging campaign before stopping the operation).The duration of the aging test of each cycle was arbitrarily set by the authors, aiming at representativeness of longer-term degradation while ensuring manageability of the aging campaign. Capacity loss at the end of the campaign is also reported in Table 2, while the full capacity loss vs EFC trend of each tested cycle, dedicatedly discussed in Ref. [17], is reported in Figure S1 of the Supplementary Materials to ease its consultation.

2.3. Characterisation procedure

The characterisation procedure involves an optimised sequence of tests to enable the identification of physical parameters with a limited set of experimental data and so limited testing time. As described in detail in Ref. [19], it includes:

Table 1
Characteristics of the experimental samples [20].

Property	Value
Manufacturer	SONY
Model	US18650V3
Nominal capacity	2.25 Ah
Voltage cut-offs	2.5V–4.2V
Electrode materials	Graphite/NMC + LMO
Continuous max charge C-rate	1C

Table 2
List of tested driving cycles with corresponding operating conditions and aging test duration.

#	Label	Temperature [°C]	Load profile	Maximum SoC [%]	Minimum SoC [%]	Charging C-rate [−]	Aging test duration [day]	Cycles at end-of-test [EFC]	Capacity loss at end-of-test [%]	#
1	WLTP 100%–0% 45 °C	45	WLTP	100 %	0 %	C/3	99	260	10.8 %	1
2	WLTP 100%–50 % 45 °C	45	WLTP	100 %	50 %	C/3	148	395	20.2 %	2
3	WLTP High-Speed	45	WLTP High-Speed	100 %	0 %	C/3	148	500	16.1 %	3
4	IEC C/3 45 °C	45	IEC 62660-1	100 %	0 %	C/3	121	530	17.7 %	4
5	IEC C/6 45 °C	45	IEC 62660-1	100 %	0 %	C/6	109	357	15.6 %	5
6	WLTP 100%–0% 25 °C	25	WLTP	100 %	0 %	C/3	162	448	9.4 %	6
7	WLTP 100%–50 % 25 °C	25	WLTP	100 %	50 %	C/3	161	419	10.7 %	7
8	WLTP 100%–75 % 25 °C	25	WLTP	100 %	75 %	C/3	159	382	7.0 %	8
9	WLTP 75%–50 % 25 °C	25	WLTP	75 %	50 %	C/3	114	301	4.9 %	9
10	WLTP 50%–0% 25 °C	25	WLTP	50 %	0 %	C/3	92	282	2.7 %	10
11	IEC C/3 25 °C	25	IEC 62660-1	100 %	0 %	C/3	109	455	9.5 %	11
12	IEC C/6 25 °C	25	IEC 62660-1	100 %	0 %	C/6	160	458	9.5 %	12
13	IEC 1C 25 °C	25	IEC 62660-1	100 %	0 %	1C	92	449	10.1 %	13

- A complete discharge at 25 °C and C/10, approximating a close-to-equilibrium condition.
- Two partial discharges at:
  - o 10 °C, 2C, from 100 % to 50 % SoC;
  - o 25 °C, 1C, from 50 % SoC to the lowest voltage cut-off.
- Two electrochemical impedance spectroscopy (EIS) measurements performed at:
  - o 10 °C, 100 % SoC, with 40 frequencies in the [4 kHz; 10 mHz] range with logarithmic distribution;
  - o 25 °C, 50 % SoC, same frequency interval as above.

EIS is performed galvanodinamically (imposing a current oscillation amplitude small enough to ensure linearity of voltage response) after at least 1 h of relaxation after the preceding charge/discharge event. The complete C/10 discharge was performed in Ref. [17] to draw the evolution of thermodynamic parameters, namely loss of lithium inventory and loss of active electrode materials. The remaining tests allow us to identify the worsening of kinetic and diffusive properties. These tests are required to identify the physical parameters of the P2D model.

The choice of this set of experimental measurements aims to shorten testing time while maximising the identifiability of the physical parameters as a result of sensitivity-based selection performed in Ref. [22].

2.4. P2D model

The P2D model is selected as a trade-off between physical consistency and computational effort to reproduce the operation of experimental samples. The model is implemented in COMSOL Multiphysics®.

A summary of the model is here presented, while all equations are listed in Section S2 of the Supplementary Materials attached to this publication. One battery cell is represented as three layers: negative electrode, separator and positive electrode. All layers are divided into solid (solid phase) and liquid (electrolyte phase) portions. The model solves partial differential equations along the main direction (i.e. orthogonal to the layers) and in the pseudo-direction, i.e. the radial direction in solid spherical electrode particles. The model includes lithium-ion transport in the electrolyte phase, lithium diffusion in solid electrodes and electron conduction in the electrodes. On the surface of the electrode particle there are three phenomena: electrochemical reaction through Butler-Volmer equation, double layer charging and film resistances (e.g. SEI). The contribution of current collectors and internal connections is included in the cell voltage through Ohm's Law. Kinetic constants of the reactions and lithium diffusivity in electrode and electrolyte phase depend on the cell temperature. Electrolyte conductivity and diffusivity constitute a single physical parameter since they are related through the Nernst-Einstein relation. Open-circuit potential (OCP) curves of the electrodes are recorded experimentally with half-cells and implemented as look-up tables.

The model is coupled with a 2D thermal model (equations in Section S2.7 of the Supplementary Materials). It computes the temperature distribution inside the cell for all the time-steps. The cell is modelled as the cross section of a cylindrical cell, with three layers: mandrel, active material and external case. Heat is produced in the active material region according to the output of the P2D model simulation. It is exchanged by conduction in the layers and by convection with ambient air at the edges. The averaged temperature of the active area is then considered by the P2D model to update the value of temperature-dependent properties, following an Arrhenius relation. For more information, the reader is referred to Ref. [22].

EIS is simulated with the P2D model both in time or frequency domain. As in the experiment, a sinusoidal current is applied at the edges of the cell and the corresponding voltage response is recorded, at different frequencies. The impedance is then computed from the ratio between voltage and current.

2.5. Parameter identification procedure

Apart from the identification of thermodynamic parameters (discussed in Ref. [17]), a selection of kinetic and mass-transport properties is estimated through a particle swarm optimisation algorithm (PSO), following a stepwise procedure. The goal of the algorithm is the minimisation of a cost function, expressed as the difference between experimental and modelled curves corresponding to the sequence of measurements described in Section 2.3, i.e. the experimental data referring to the test sequence of Section 2.3 are the input information to the algorithm (training dataset) and the algorithm aims at making

models simulation in agreement with this set of measurements. The algorithm spans a very broad solution space. It starts with random initialization and along iterations it progressively approaches the minimum. Along the iterations, some logics are implemented to guide the algorithm towards the minimum, exploiting all the explored solutions of all particles at all previous iterations depending on their level of reliability (i.e. the value of the associated cost function). The parameters to be identified are kinetic rate constant and solid-state lithium diffusivity for positive and negative electrodes, ionic conductivity of the electrolyte, SEI resistance and double-layer capacitance of the positive electrode.

The process involves four steps. In the first, LLI and LAMs are identified by simulating a complete C/10 discharge. LLI and LAM affect the amount of cyclable lithium and the electrode volume to host lithium, respectively. Thus, in turn, the stoichiometry at beginning and end of discharge [19]. For the purpose of this work, LAM is considered as purely delithiated, thus a loss like LAM of one electrode does not induce a reduction of cyclable lithium. This solution ensures more flexibility, since LAM can occur at different SoCs and so it can induce a different amount of lithium loss. The effect of a lithiated LAM can be suitably reproduced by the superposition of LLI and delithiated LAM [19]. On the other hand, LLI is associated only with a loss of cyclable lithium, without altering the electrode structure. To shorten simulation time, LLI and LAM are identified exploiting a simplified model. Since their identification is part of a previous publication [17], the model is not described here, but the equations are made available in Section S3 of the Supplementary Materials.

In step 2, kinetic properties are identified by reproducing the EIS spectra reported in the procedure of Section 2.3 at best. Similarly, diffusive properties are estimated in step 3 from partial discharge curves of Section 2.3 and, finally, step 4 consists in a refinement phase, by repeating step 2. The algorithm is applied in each of these steps, exploiting different cost functions. In all steps, the number of particles was 25 times or 50 times the number of fitting parameters and iterations were at least 10. One full parameter identification procedure requires 60h on average on a standard desktop computer.

The selection of the characterisation procedure, algorithm logics and of the fitting parameters was performed in previous publications [19, 22]. The analysis started from a one-factor-at-a-time sensitivity analysis, where 28 model parameters were investigated by analysing the variation of the model response due to each parameter change. This change, in turn, was evaluated at different operating conditions (e.g. temperature, C-rate, frequency of EIS excitation, …) and different test type (discharge, EIS and relaxation after discharge). This work enabled to identify a reasonable solution to:

- shorten testing time (few tests, easy to combine experimentally);
- select useful fitting parameters (parameters which poorly affect the model response are considered constant and equal to a literature value);
- select meaningful fitting parameters (all the most important phenomena are considered, not to bias the solution and keep the tool flexible);
- increase model parameters identifiability (choice of suitable operating conditions);
- ease the optimisation problem (by understanding the interplay and possible mis-interpretation due to different parameters providing similar model response).

The reader is referred to Refs. [19,22] for more details.

The algorithm estimates single effective properties. Indeed, the operation is characterised by gradients of performance along the through-plane direction and the jelly roll direction already at the fresh state, with possible additional heterogeneities due to heterogeneous degradation. However, this complex behaviour is reproduced by the P2D model with single effective properties due to its 1D nature. As a consequence, parameter evolution is not representative of the variation of the parameter itself but of the tendency towards the worsening of classes of phenomena. For instance, a reduction of the electrolyte conductivity of 50 % can be associated with local spots, characterised by strong degradation, while the average loss is lower than 50 %. Moreover, since only a subset of parameters is identified, the variation of one parameter can be the result of different sources. In the case of electrolyte conductivity, a variation of local porosity can result in an apparent worsening of the electrolyte properties since the path for ion transport in the electrolyte phase becomes more resistive.

The parameter identification results are provided as a “best fit” with a confidence interval for each parameter. “Best fit” values correspond to the solution which minimises the cost function of the algorithm. However, since many solutions can provide very similar results in the simulation of training measurements, a confidence interval is added to consider this variability. Confidence bands are not related to the experimental uncertainty of the measurements, even though it could further increase the uncertainty of the results.

All solutions, whose cost function is up to 5 % larger than the “best fit” value (e.g. the lowest cost function value), are considered as “best solutions”. 5 % is arbitrarily selected after a preliminary analysis: below 5 % the differences in the model simulations are so limited that the solutions can be reasonably considered as equal. As a consequence, they are considered able to reproduce the experimental trends with equal reliability. Therefore, confidence bands of a prescribed parameter A include all the values the A takes in the “best solutions”. The lowest value of A in its confidence band refers to the lowest value of A within the best solutions population. The same reasoning holds true for the maximum value.

This interval enables to assess whether the variation of one parameter due to degradation is meaningful. In case of a clear trend, it is possible to state that there is a connection between this parameter and ageing, due to one or more degradation phenomena. It is worth noting some complexities of this representation, like:

- The capability of the P2D of simulating aged cells performance, also considering the limited amount of input data (see Section 2.3) to save testing time. The more challenging the experimental data, the larger the uncertainty on the parameters value.
- The identifiability of each parameter. If one parameter is poorly affecting the model response (e.g. voltage value along a discharge), its estimation shows a large confidence band.
- Confidence bands do not show the distribution of the solutions. One solution with one extreme value is enough to add this value in the tolerance, even though it could appear like an outlier.

The tool works in this way for the sake of simplicity and universality. The results for its application on the fresh cell are reported in Tables S1 and S2 of the Supplementary Materials.

For additional information on the methodology, the reader is referred to Ref. [19].

2.6. Post-mortem analyses

One fresh and two cycled cells are opened in an inert environment at the end of life to undergo post-mortem analyses. Coin cells are built with material harvested at several positions along the roll, to perform C/50 q-OCP cycles through a Neware BTS4000-5V10mA (10 mA maximum current per each channel) battery testing system at 21 °C and EIS by means of either Gamry Reference 3000 or Gamry Interface 5000E potentiostats at 25 °C and every 5 % or 10 % SoC levels, consistently as performed in Ref. [18]. Moreover, Scanning Electron Microscope (SEM) is performed with different magnifications to visualise the size and shape of electrode particles and the presence of layers on the surface. Lastly, possible variations in chemical composition are investigated by means of Energy Dispersive X-ray Spectroscopy (EDS).

3. Results

The IEC cycle at 25 °C with C/3 recharge C-rate is selected as a reference case to identify the general evolution of the physical parameters. Its cell capacity loss vs EFC is reported in Figure S1a of the Supplementary Materials (blue curve). Thermodynamic parameters decay was already identified in Ref. [18] and is reported here for comparison when needed.

3.1. Experimental trends

The dashed lines in Fig. 1 show the evolution of EIS and high C-rate discharges as part of the periodic characterisation procedure (see Section 2.3).

- **EIS:** Nyquist plots (reported in Fig. 1a and c) show how the spectra undergo notable changes throughout the campaign. Initially, the fresh cell exhibits a single elongated semicircle, whereas degradation leads to the emergence of two distinct features. Bode plots of imaginary component of the impedance (Fig. 1b–d) allow to further investigate such changes: within the frequency range of 30Hz–1000Hz, a sudden alteration occurs already at early aging stages, followed by a stabilisation. Additionally, a new low-frequency kinetic loop emerges and steadily increases with ageing. Comparison between EIS1 (100 % SoC, 10 °C in Fig. 1a and b) against EIS2 (50 % SoC, 25 °C in Fig. 1c and d) permits to further correlate this variations with test conditions. Indeed, in Fig. 1a and b impedance remains relatively unchanged in the last stages, contrasting with the variations observed in Fig. 1c and d, where the additional feature at low frequencies is still progressively shifting towards a frequency lower than 1Hz at the end of the campaign. Hence, at the characteristic frequency of the phenomenon increases with increasing temperature, as discussed further in Section 4.1.
- **DISCHARGE:** From the 10 °C 2C discharge (Fig. 1e) test emerges a marked transient at the beginning of discharge, with a quite steep profile which then stabilises into a linear trend. This change progressively strengthens with ageing and, after ~200 equivalent full cycles (EFCs) tends to flatten. Overall, there is a growth of the polarisation losses, growing up to 200 mV between the fresh sample and the last ageing stages. Lastly, the low SoC discharge at 25 °C and 1C (Fig. 1f) highlights with ageing the capacity reduction and voltage losses growth. Moreover, the last part of the discharge becomes less steep, which could be related to a diffusive limitation.

3.2. Modelling results

The model is exploited to perform PSO-based parameters estimation on the tests presented in Section 2.3 and to understand the ageing

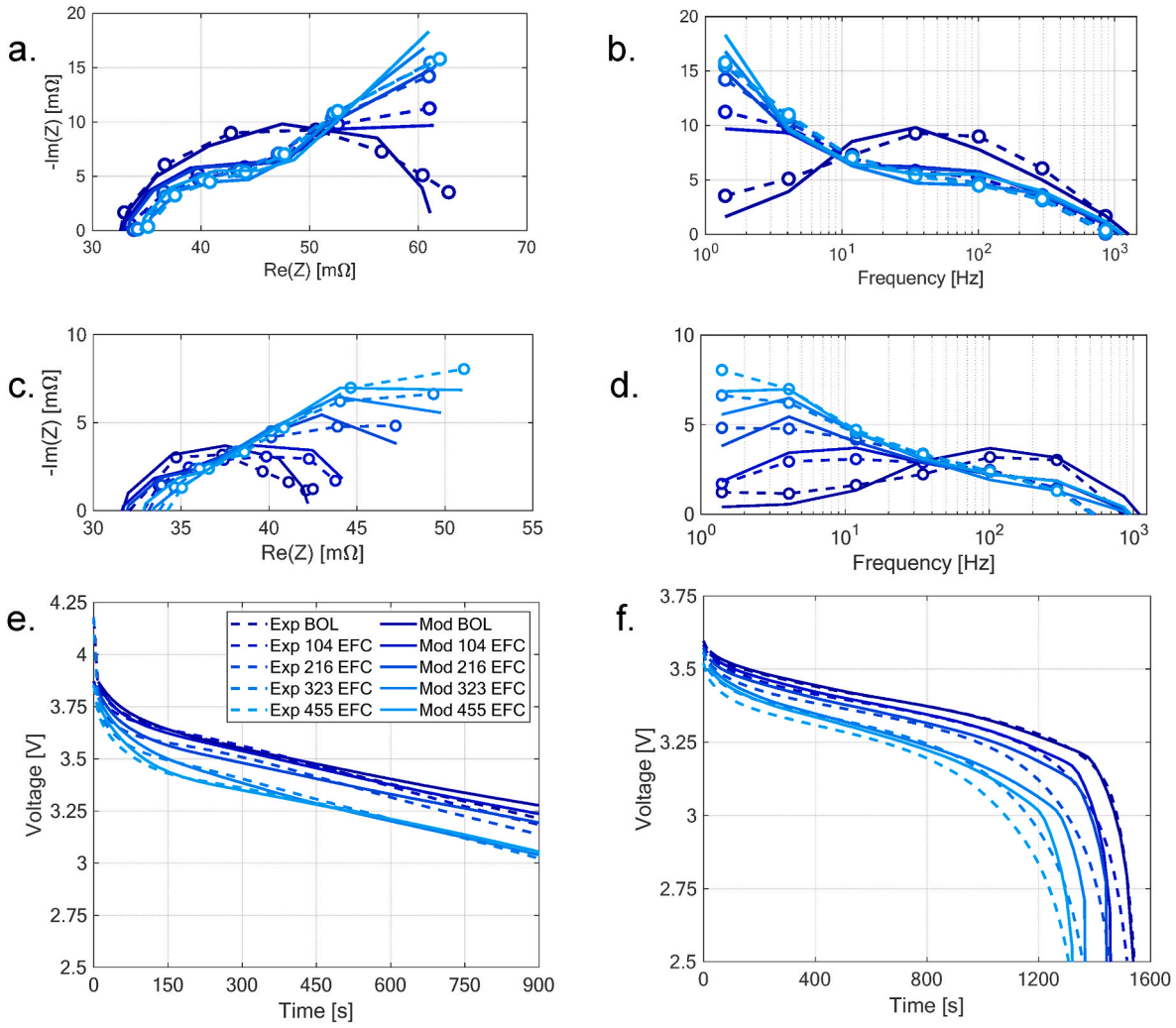

Fig. 1. Experimental (dashed lines) and corresponding simulations (full lines) of the characterisation procedure tests for the cell cycled at 25 °C with IEC profile: Nyquist and Bode plot of the imaginary component of the impedance at 100 % SoC and 10 °C (a–b) and at 50 % SoC and 25 °C (c–d); discharge from 100 % to 50 % SoC at 10 °C 2C (e) and from 50 % SoC to the minimum voltage level (f).

behaviour. The resulting simulations are reported in full lines in Fig. 1. Simulated EIS reproduce the experiments reliably at both 100 % SoC 25 °C (Fig. 1a and b) and 50 % SoC 10 °C (Fig. 1c and d). The error in high-frequency intercept (or high-frequency resistance, HFR) simulation is lower than 1 mΩ and both magnitude and characteristic frequencies of the kinetic loops match in a satisfactory way at all ageing states. Similarly, the relevant variations of both the simulated discharges (Fig. 1d and e) are satisfyingly reproduced, especially for the discharge 100 %–50 % SoC at 10 °C and 2C, where the evolution of initial transient followed by the flattening of the is well captured. Regarding the discharge

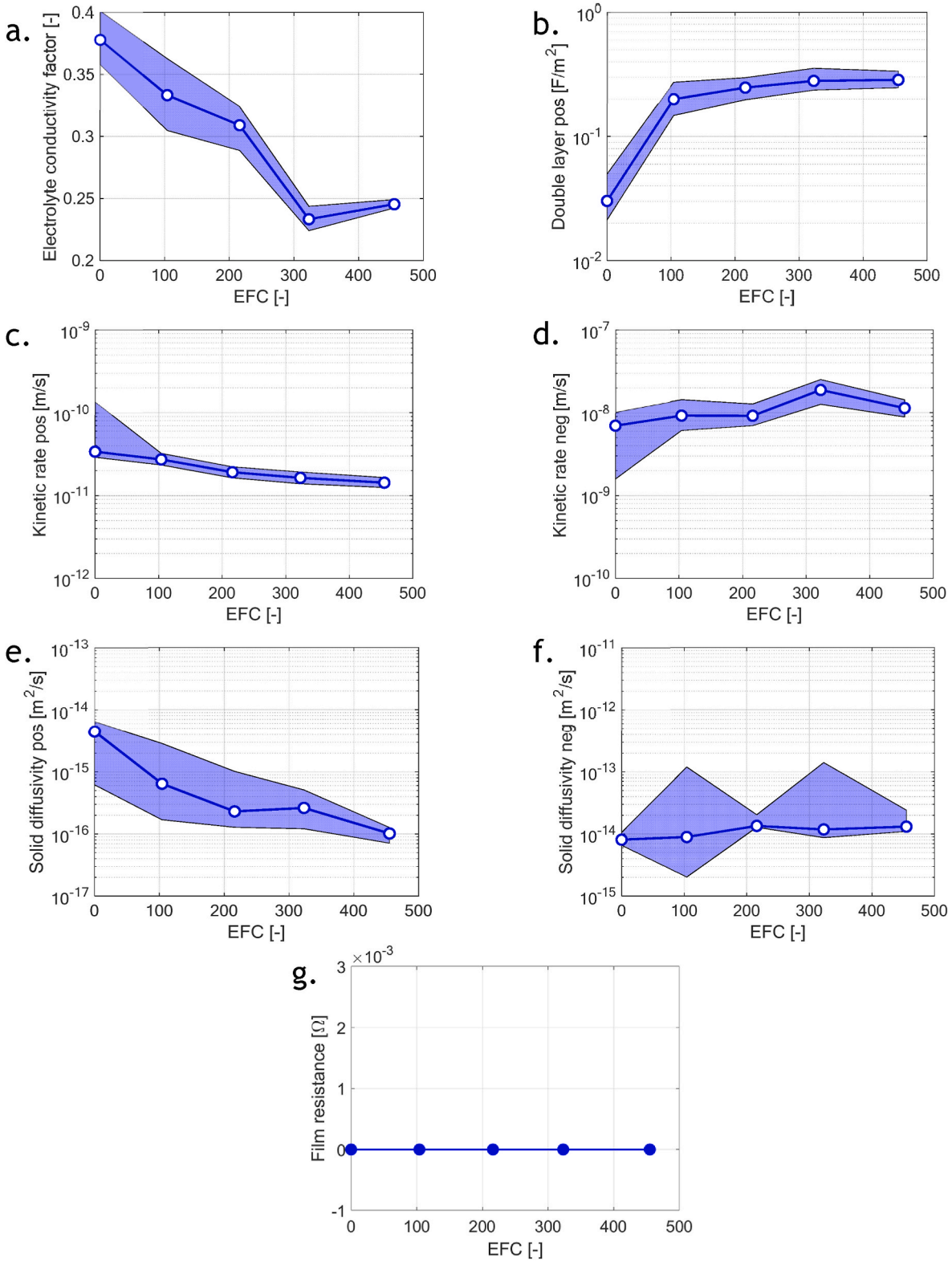

Fig. 2. Trend of physical parameters over EFC with uncertainty bands: a) electrolyte conductivity factor, b) positive electrode double layer capacitance, kinetic rate constant of c) positive and d) negative electrodes, solid-state diffusivity of e) positive and f) negative electrodes, g) negative electrode film resistance.

from 50 % to 0 % at 25 °C and 1C, the voltage profile and capacity reduction trends show good agreement with the experimental.

A decrease of model reliability at increasing aging state is noticeable especially at lower SOC, as common in the literature [23]. The quality of the results has to be evaluated considering the framework and objective of the work. First, the set of free parameters to be identified is restricted in order to reduce the computational effort on one side, while preserving physical consistency and ensuring the model the capability of reproducing major aging trends. Increasing parameters number would increase the capability of the model as well as computational burden. Moreover, the amount of input experimental data is also limited to two partial discharges and two EIS, to optimise the process. More input information would improve the parameter identification problem. Lastly, despite the little input information, the operating conditions are wide in terms of C-rate, temperature, state of charge, resulting challenging. Further improvements may be obtained, e.g. considering a variable solid diffusivity with respect to lithiation of the electrodes. These solutions, however, would affect the compactness of the method and would be out of the scope of the present work. All in all, this result is considered well satisfying.

Therefore, an investigation of the trend of identified parameters is performed. The results of the algorithm are reported in Fig. 2 and hereby discussed.

3.2.1. Trend of kinetic parameters

An almost linear drop in electrolyte conductivity is estimated (Fig. 2a). This parameter is of primary importance during discharge and is responsible for most of the voltage drop. Its effect is detectable in the high-frequency intercept and in the charge-transfer region of the impedance [8]. Then, the algorithm associates the high-frequency loop of the impedance with the charge transfer phenomenon of the negative electrode. Since this loop is unchanged during the campaign, the corresponding kinetic rate (Fig. 2d) remains constant. (This stability arises from the assumption on the double-layer capacitance discussed in Section S5 of the Supplementary Materials). On the contrary, the double-layer capacitance of the positive electrode follows the frequency shift of the loop. Indeed, there is a rapid growth of capacitance, lowering the characteristic frequency of the charge transfer mechanism, which then almost stabilises. The rate constant has a steady decrease, resembling the trend of the magnitude of the low-frequency feature, which continues to increase (as noticeable in Fig. 1c). Similar impedance evolution was already observed in the literature and was already consistently attributed to the positive electrode charge transfer [8,24–26].

3.2.2. Trend of mass-transport parameters

Lithium solid-state diffusivity into graphite (Fig. 2f) has a slightly growing trend. This parameter is closely related to capacity retention at different C-rates. The extractable capacity in a full discharge at 1C is less affected by degradation than the C/10 one (see Figure S.6 of the Supplementary Materials). This experimental fact forces the diffusivity to grow. This trend stabilises, as LAMn does (see Figure S.7 of the Supplementary Materials). These parameters might be correlated, suggesting a form of stabilisation of the material. One interpretation for this trend could be found in a progressively smaller solid particle radii, favouring lithium diffusion. Since particle radii are kept constant in the parameter identification process, this effect translates into a variation of the effective diffusion property. Consistently, as the active area is also affected by the particles size, a similar effect should be expected to occur on the kinetic constant. As a matter of fact, the characteristic time of diffusion is proportional to the radius, while the active area grows with the inverse of the radius.

On the other hand, Lithium diffusivity in the positive electrode strongly decreases (Fig. 2e). This effect becomes particularly relevant in the 10 °C and 2C discharge (Fig. 1e), where it is suspected to cause the occurrence of the voltage plateau, which is now discussed in detail.

3.2.3. Heterogeneous electrode utilization due to aging

The decay of physical properties sensibly impacts the performance also from an heterogeneous materials utilization perspective. In the following, a deepening of the dynamics of the 2C 10 °C discharge is performed to discuss this effect and demonstrate the capability of the model to reproduce and explain the complex operation of an aged cell. The simulation refers to the end-of-campaign state of the cell cycled with IEC at 45 °C. Fig. 3a shows the voltage profile in time, while Fig. 3b–c show the evolution of both local reaction rate and lithium concentration against the through-plane direction at several time instants (from 0 to 900 s) along the discharge.

As noticeable, at the beginning of discharge most of the reaction is localised in the area close to the separator (see Fig. 3b at 18s and 135s) of both electrodes because of the low electrolyte conductivity. Consequently, there is a progressive shift of the local reaction rate towards the current collector area (Fig. 3b). As soon as graphite is locally delithiated (Fig. 3c), the equilibrium potential and reaction overpotentials force the reaction to occur elsewhere electrode utilization to increase.

Both electrolyte conductivity and lithium solid-state diffusivity in positive electrode are very low, while solid-state diffusion in graphite is not limiting. This is very clear in the evolution of local gradients: lithium concentration on the surface (full lines in Fig. 3c) and in the center (dashed lines in Fig. 3c) is almost the same for graphitic particles (left-end side in Fig. 3c), while significant gradients exist in the positive electrode (right-end side in Fig. 3c), especially at the interface with the separator. At 900s (e.g. at a nominal 50 % SoC, red curve in Fig. 3c), lithium concentration in the electrode becomes saturated close to the separator, forcing lithium ions to reach the middle of the electrode thickness to intercalate, further increasing transport losses.

The low diffusivity in the positive electrode plays a key role in defining the shape of the voltage curve, as reported in Fig. 3a. In the first 2 min, there is an initial drop related to ohmic and kinetic losses, followed by a linear trend. This loss is due to the heterogeneous utilization of the positive electrode: the local lithium concentration (Fig. 3c) varies fast and, correspondingly, analogous behaviour is found for the equilibrium potential (Fig. 3a). After that, lithium starts to diffuse in the solid phase (Fig. 3c, between 135s and 360s) and the OCP associated with the local concentration in the area close to the separator approaches a flat region. This combined effect leads to the flattening of the curve.

No major role of self-heating is taking place because the time scale is relatively short. This consideration was verified by a dedicated experiment (reported in Section S7 of the Supplementary Materials), performing the same discharge three times with different heat convection fluxes on the surface of the cell: temperature is important to define the property of the material at the beginning of discharge while self-heating becomes relevant only after few minutes.

3.3. Degradation interpretation

Electrolyte conductivity is found to decrease linearly with cycles. It is possible to derive that relevant consumption of the electrolyte is evident, either to form SEI or release gases [1,8,26–28]. SEI is expected to grow in all the cells, though with different rates and properties. Electrolyte decomposition is also responsible for a significant share of impedance rise [1,26] and of overpotentials in the discharge [11,29].

At positive electrode, the kinetics of the reaction and its solid-state diffusivity are estimated to be worsening.

- Diffusion limitations are seldomly investigated [30], but X. Zhou et al. [29] combined the distribution of the relaxation time method and physics-based modelling to analyse the EIS of an NMC|Graphite cell and they identified a significant decrease of diffusion coefficients in both solid and, mainly, electrolyte phases due to ageing at 45 °C, without providing a clear explanation. V. J. Ovejas et al. [31] observed a solid-state diffusive limitation on the positive electrode half-cell due to ageing and related it to the occurrence of phase

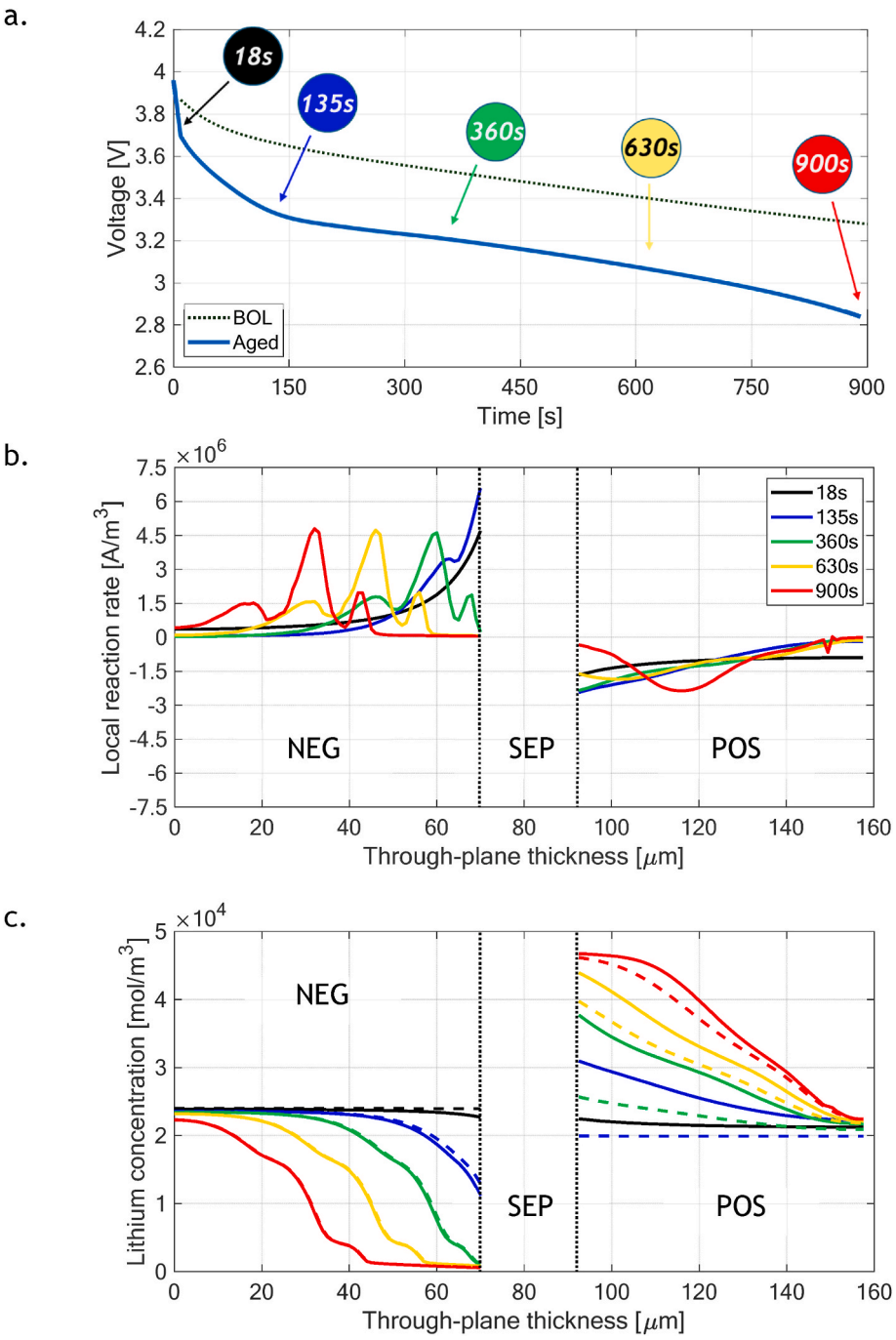

Fig. 3. Model simulation of aged cell cycled with IEC at 45 °C performing discharge 100 %–50 % SoC at 10 °C 2C. a) Voltage profile, highlighting specific time instants at which is shown: b) Volumetric current over electrode thickness. c) Lithium concentration on the surface (full lines) and center (dashed) of electrode particles.

transitions, but they did not provide a physical explanation for its worsening due to ageing. L. Zhang et al. [11] with a modelling analysis, estimated the worsening of solid-state diffusive properties of both electrodes without explaining the physical origin of this trend.

- Different mechanisms might be in play regarding kinetics. In general, a worsening of cathode charge transfer has been observed in the literature on layered NMC electrodes [6,8,24–26], but a physical interpretation is only seldom provided. P. S. Sabet et al. [24] identified the following list of possible mechanisms: cathode electrolyte interphase (CEI) formation, cathode dissolution, cation mixing and particle cracking, which is in agreement with [1]. V. J. Ovejas et al. [25] observed an increase in the double-layer capacitance of the positive electrode of cycled cells coupled with an increase in its charge-transfer resistance. They proposed that particle cracking and corresponding film formation caused the resistance increase and that the increase of the double layer capacitance was due to a slower reaction kinetics, which caused an accumulation of ions and salt at the electrode-electrolyte interface, compressing the double layer which, in turn, had a larger capacitance. Moreover, G. Liu et al. [32] demonstrated how the interaction between active material, conductive additives and binder significantly affects the electrode impedance. Later, J. M. Foster et al. [33] showed how cycling can lead to binder delamination and H. Liu et al. [34] revealed how

detachment between active material and binder can lead to loss of conductivity, which can partially justify the capacity loss trend.

At negative electrode, although lithium plating might take place on very aged cells [8,35], no tests suggest its occurrence in any cell of this campaign.

Overall, the results are in line with the literature and the model proved to be a valuable tool to inspect and understand the behaviour of aged cells. However, it is hard to sort out the most likely phenomena related to the positive electrode due to little knowledge on one side and many different phenomena on the other. Consistently, all the measurements show a progressive evolution.

3.4. Effect of operating conditions

To identify the impact that different automotive-related operating conditions may determine on battery degradation, subsets of the different aging cycles are selected to enable meaningful comparisons. Such subsets, each sharing specific operating parameters, are singularly discussed in the following sections. To recall capacity loss vs EFC of each tested cycle, dedicatedly discussed in Ref. [17], reader is again addressed to Figure S1 of the Supplementary Materials.

3.4.1. Effect of recharge current

First, the effect of the recharge current is investigated by comparing the aging of the cycles that share all the operating conditions but the recharge C-rate, namely:

- IEC cycle at 25 °C, between 100 % and 0 % SoC, with 1C recharge C-rate;
- IEC cycle at 25 °C, between 100 % and 0 % SoC, with C/3 recharge C-rate;
- IEC cycle at 25 °C, between 100 % and 0 % SoC, with C/6 recharge C-rate.

The same approach is then applied in the following sections.

In [17], the evolution of capacity loss and thermodynamic parameters was the same for all three cycles cells. Similarly, mass-transport and kinetic parameters appear to vary in the same way (Fig. 4b and c). All considered cycles exhibit a relevant, yet comparable, reduction of conductivity and their evolution over EFC is very similar. Such decrease in electrolyte conductivity, as visible from Fig. 4a, can be considered a proxy for side reactions like SEI growth. Similarly, mass-transport and kinetic parameters appear to vary analogously in the same way as visible from Fig. 4b and c, where the evolution of the kinetic rate constant and lithium solid-state diffusivity of the positive electrode are depicted.

Summarizing, also for these parameters, the evolution is not affected by the recharge C-rate at a significant level.

Hence, this analysis further supports the observations in Ref. [17], suggesting that the recharge C-rate was identified as almost irrelevant to the ageing trajectory in the investigated range [C/6; 1C] and for the battery type under investigation. It is worth highlighting that 1C is the maximum continuous charge C-rate recommended by the manufacturer and that 25 °C is reasonably high enough to ensure that no lithium plating is taking place. Increasing the value beyond operational limits would have led to operational misuse, whose effects evaluation is of the scope of the present work.

3.4.2. Effect of load profile

This section highlights the effect of the load profile, comparing the following cycling conditions:

- the IEC cycle at 25 °C, with C/3 recharge and 100%–0% SoC window;
- the WLTP cycle at 25 °C, with C/3 recharge and 100%–0% SoC window.

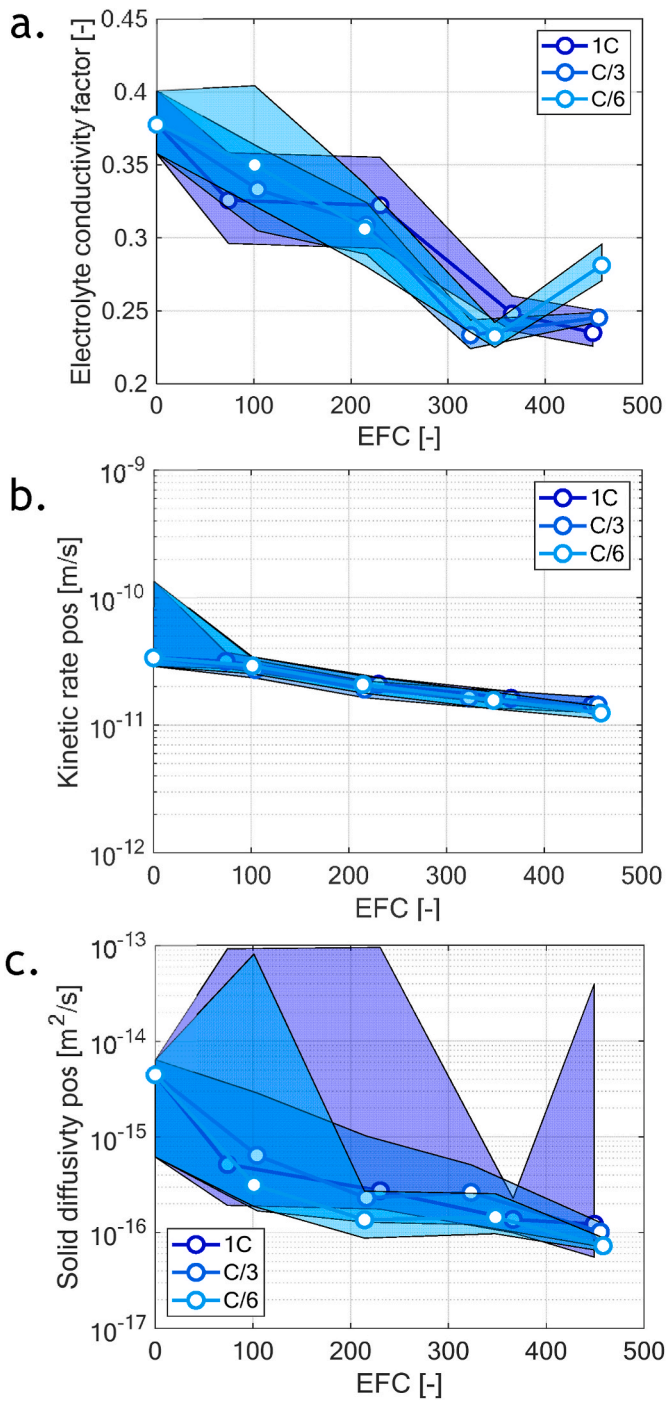

Fig. 4. Effect of recharge C-rate: trend of selected physical parameters over EFC for cells cycled with IEC cycles at 25 °C and different recharge C-rates, with uncertainty bands: a) electrolyte conductivity factor, b) kinetic rate constant and c) solid-state diffusivity of the positive electrode.

The differences between the profiles were summarised in Section 2.2. In Ref. [17], the load profile did not provide significant effects on capacity loss (as visible from Figure S1 of the Supplementary material) nor on q-OCP degradation.

Analogously, the EIS of both cells shows the evolution of same features at the same pace. As a result, kinetic properties follow the same evolution: Fig. 5b reports the kinetic rate constant of the positive electrode, as an example. In the last stages, a slight difference occurs in mass transport parameters: with respect to WLTP, IEC cycle apparently leads to a slower decay for lithium diffusivity in the positive electrode (Fig. 5c)

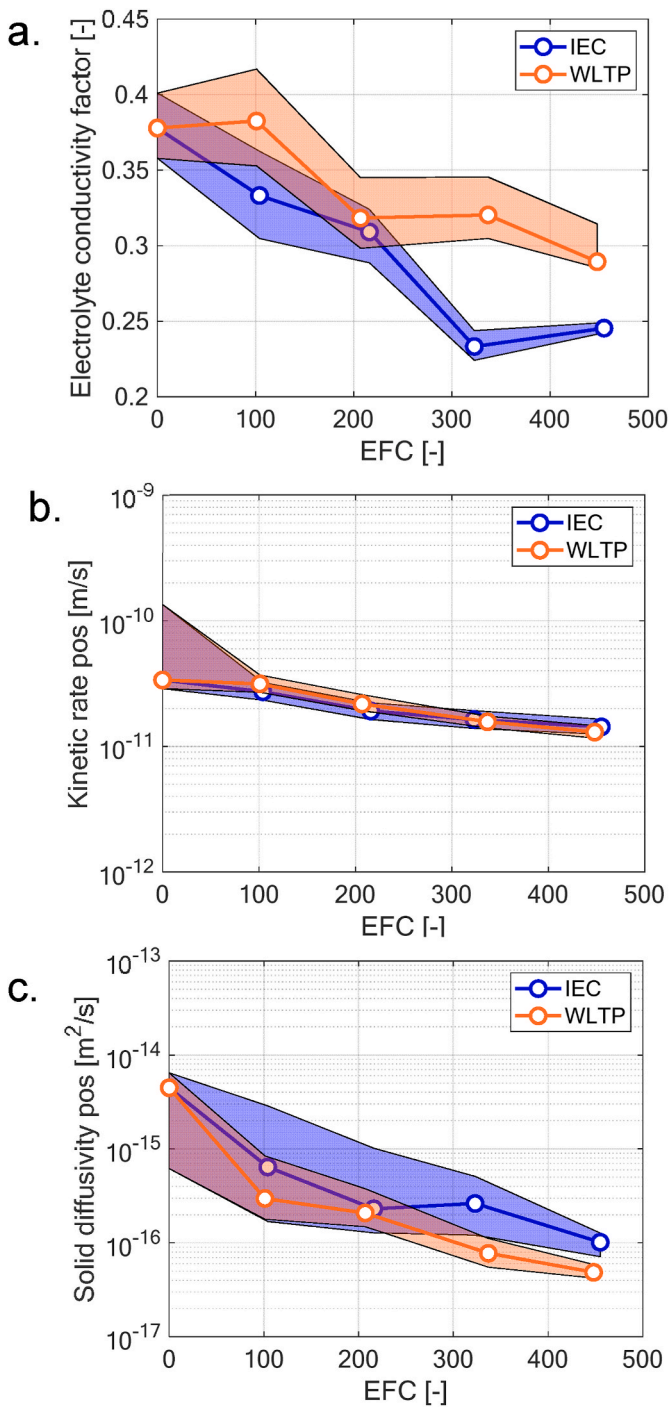

Fig. 5. Effect of the load profile: trend of selected physical parameters over EFC for cells cycled with IEC and WLTP cycles at 25 °C, with uncertainty bands: a) electrolyte conductivity factor, b) kinetic rate constant and c) solid-state diffusivity of the positive electrode.

and to a slightly faster decay for electrolyte conductivity (Fig. 5a). However, it is worth underlying how on very aged cells the effect of these two parameters on cell operation is similar enough to be mistaken on for the other up to a certain extent, as one can partially counterbalance the effect of the other. In our case, indeed, only a slight difference exists in the experimental data collected through the characterisation procedure; thus, it is reasonable to assume there is little difference between the effects of the two cycles when very aged. IEC is characterised by sensibly higher currents, both in discharge and in regenerative events, which may trigger gas evolution, consuming additional electrolyte material while lithium loss is unaffected, however it is impacting cell performance roughly as the WLTP cycle. No clear explanation is proposed for the solid-state diffusivity trend.

An additional comparison is reported between WLTP, IEC and WLTP High-Speed profiles at 45 °C (Figure S.9 of the Supplementary Materials). Their parametrisation is not performed since their strong similarity is very clear from the experimental data. As an example, the differential voltage and 10 °C 2C discharge are depicted, as part of characterisation procedure. The curves overlap if considered at similar EFC values. This result further supports the limited effect of this variable on degradation.

In conclusion, there is no large difference in degradation due to the investigated loads, despite ageing being known to be path-dependent [36,37]. Additional electrolyte degradation is observed for the IEC cycle, possibly related to gas release. This analysis interestingly supports the use of IEC as representative of real-world degradation, providing a beneficial effect for laboratory tests since it enables faster experimental campaigns with respect to the WLTP profile.

3.4.3. *Effect of state of charge window*

To highlight the effect of this variable on degradation, Fig. 6 shows the evolution of several physical parameters for three different cycles at 25 °C with C/3 recharge current, namely:

- WLTP within the 100%–0% SoC window (red curve);
- WLTP within 100%–50 % SoC window (orange curve);
- WLTP within the 100%–75 % SoC window (yellow curve).

In [17], both LAMp and LLI were found to vary with average state of charge and with depth of discharge (DoD) of the cycle. In particular, LAMp grows with DoD, suggesting the occurrence of particle cracking, while LLI, proportional to average SoC, was associated with SEI growth.

In Fig. 6a, the evolution of the electrolyte conductivity is reported, demonstrating no significant difference among the effects of the three cycles, as the uncertainty bands almost overlap. This result is unexpected, since high SoC is usually associated with promoted side reactions such as SEI growth. However, this fact might be related to the maximum SoC of the cycle (SoC 100 %), which is shared by all the cycles. Due to the narrow level of degradation of the low SoC cycle (not reported in Fig. 6), no further verifications are allowed.

Nevertheless, Fig. 6d shows the trend of SEI film resistance: its value is close to zero at the beginning, while afterwards it grows linearly with EFCs. It is interesting to observe how the onset and magnitude of this parameter's growth are proportional with the DoD of the cycle. In the selected cycles, since all start at SoC 100 %, having low DoD implies cycling at a higher average SoC, which is known to promote SEI. Decoupling these variables would require additional testing conditions and is out of the scope of the present investigation, focusing on automotive-relevant operation, so a following work is suggested to investigate the missing combinations of operating conditions. However, it is worth underlying how the 100%–50 % at 45 °C shows a steeper loss of electrolyte conductivity and faster growth of the film resistance with respect to the behaviour of 100%–0% SoC cycles. Therefore, it is possible to state that the dependence of these parameters on DoD and SoC is significant.

Lastly, Fig. 6b and c reports the parameters of the positive electrode (kinetic rate constant and lithium bulk diffusivity). Their decrease seems promoted by the DoD, as it was identified for LAMp [17], hence they might be related to particle cracking or additional degradation phenomena.

To summarize, depth of discharge and state of charge are interconnected and further combinations of conditions would be necessary to identify their effects with more confidence. However, following interpretation is proposed: deteriorated kinetics and sluggish diffusion could be dependent on the DoD and SEI resistance could be dependent on the average/maximum SoC or DoD.

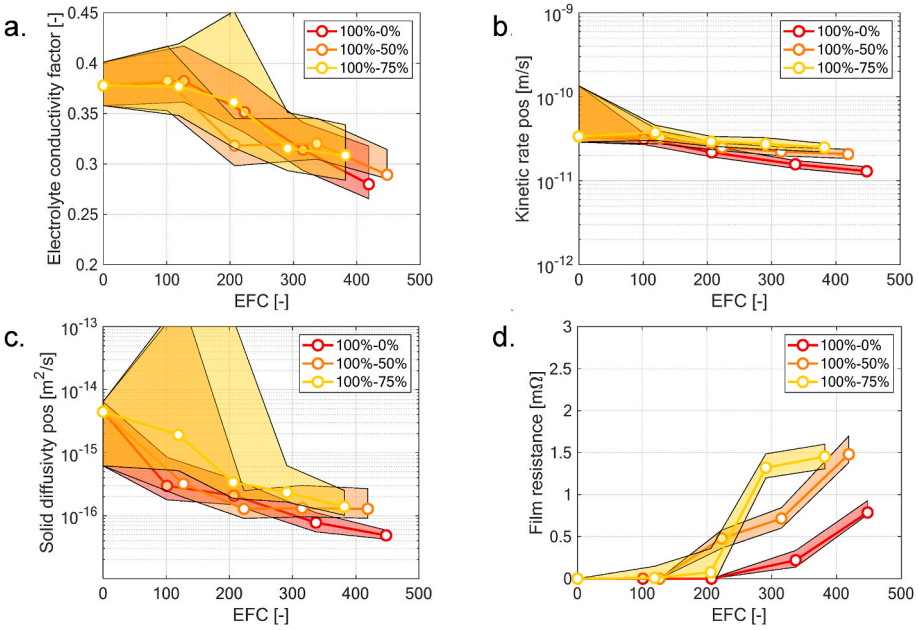

Fig. 6. Effect of SoC and DoD: trend of selected physical parameters over EFC of cells cycled with WLTP cycles at 25 °C, working within different SoC windows, with uncertainty bands: a) electrolyte conductivity factor, b) kinetic rate constant and c) solid-state diffusivity of positive electrode, d) negative film resistance.

3.4.4. *Effect of temperature*

In [17], it was observed that the superposition principle holds true at the thermodynamic level, meaning that the evolution of one parameter of a high-temperature cycling campaign was suitably reproduced by the superposition of the trends of the same cycle but performed at 25 °C, and the calendar-aged cell at high-temperature, stored at the intermediate SoC swept by the cycle. The investigation of kinetic and mass-transport parameters is reported here.

Fig. 7 reports the evolution over time of parameters which are related to kinetics and mass transport phenomena for the same set of cells. Charts are restricted up to 120 days to improve readability. In general, it is clear how calendar ageing induces lower degradation rates than cycling. For instance, the electrolyte conductivity (Fig. 7a) decreases sensibly for the calendar-aged cell but over roughly three times the period of the cycled cells. In the time span of the cycles, the evolution of the calendar campaign is slower. On the contrary, degradation seems poorly affected by the cycling temperature. The trend of electrolyte conductivity is similar, and the same observation holds true for the positive electrode properties (Fig. 7b and c for kinetic rate constant and solid state diffusivity, respectively). While the solid state diffusivity will decrease at a similar extent for longer periods, the kinetic constant is quite stable for the calendar cell, as already noticed in Ref. [17]. The only difference is related to the film resistance (Fig. 7d). It comes from the quite different value of the HFR, measured through EIS. As already mentioned, it can be related to the growth of the SEI. Its stronger growth at 45 °C is consistent with the theory. It is also present

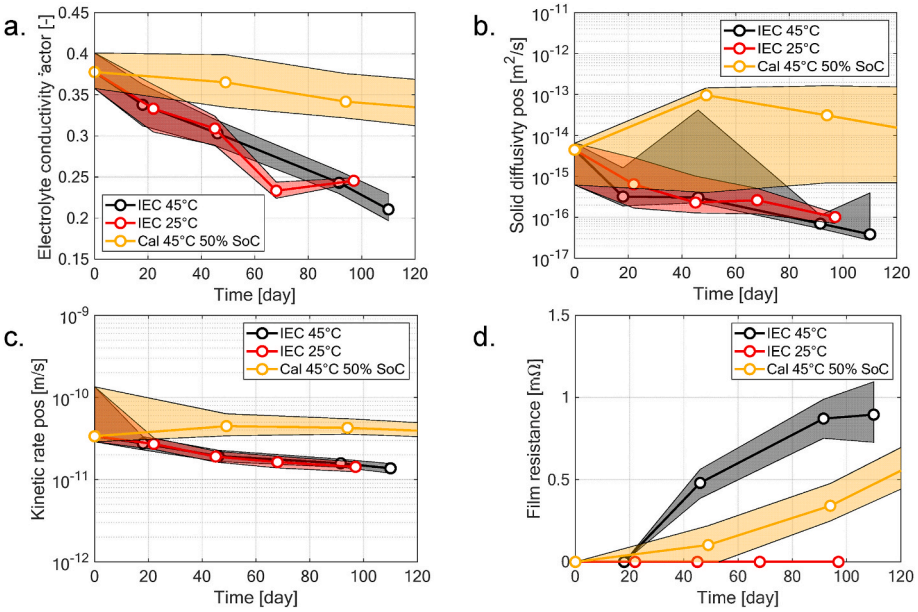

Fig. 7. Effect of the temperature: trend of selected physical parameters over EFC for cells cycled with IEC cycle at 25 °C and 45 °C and calendar aged cell at 45 °C and 50 % SoC, with uncertainty bands: a) electrolyte conductivity factor, b) kinetic rate constant and c) solid-state diffusivity of positive electrode, d) negative film resistance.

in the calendar cell, but a direct superposition of the effect is not allowed for this parameter.

A second comparison is reported for the sake of the universality of the analysis. Indeed, the cycled cells with WLTP in the 100%–50 % SoC window at 25 °C and 45 °C are compared in Figure S.10 of the Supplementary Materials. The main difference refers to the electrolyte conductivity, where WLTP at 45 °C shows a steeper profile. It might be related to a larger side reaction rate. However, it is not coupled with a thicker SEI since the film resistance is similar.

This analysis shows the prevailing role of cycling in the evolution of kinetic and mass transport-related parameters. The only difference is in the trend of the negative electrode film resistance, which is consistent with a temperature-driven SEI growth. This trend is also consistent with the larger LLI that is experienced by the 45 °C cycled cell [17]. The thermodynamic analysis holds true for all the tested couplings, while the trends in electrolyte conductivity and film resistance seem cycle-dependent. Therefore, no generalisation is allowed on the degradation of the electrolyte.

3.4.5. *Final remarks on the role of the operating conditions*

An extensive campaign is conducted under varying operating conditions, and the models are applied to understand the experimental trends. After the analysis of an example, a deepening of the effect of the operating conditions is performed. In particular, after the detailed discussion on degradation effects of different operating conditions, few interesting points can be summarised:

- The analysis of kinetic and mass-transport parameters confirms that, unexpectedly, there is no significant difference in ageing between C/6, C/3 and 1C recharge C-rate cycles in any of the investigated parameters.
- Minor differences are associated with the choice of the load profile. In this activity, the IEC cycle, characterised by higher C-rates, is related to additional electrolyte degradation with respect to the WLTP cycle, which shows a larger worsening of solid-state diffusion of the positive electrode. IEC appears as a consistent cycle to accelerate automotive-related degradation.
- DoD and SoC might be detrimental to kinetic and diffusive properties of the positive electrode, as already observed for LAMp. SEI resistance is also affected, but additional cycle conditions are required to decouple the DoD and SoC effects.
- In general, calendar ageing proved to be much slower than cycle ageing, whose dependence on the cycling temperature is limited. The evolution of the kinetic and mass-transport parameters is poorly affected by the cycling temperature, apart from the film resistance of the SEI promoted by high temperatures.

4. Validation of the results

Additional measurements are performed at the end of the aging campaign to verify the meaningfulness of the analysis. This set of information is exploited as a validation, i.e. no data are exploited to perform the parameter identification. Only EIS is exploited to state that the double-layer capacitance at the negative electrode could be kept constant, as explained in Section S5 of the Supplementary Materials. As a consequence, modifications on the surface of the positive electrode might have taken place.

4.1. *Simulations of the validation dataset*

The first verification method is the simulation of a wide set of conditions outside the training dataset to verify the reliability of the calibrated model. Fig. 8 reports the results of the discharges and EIS under several operating conditions (in terms of temperature, C-rate and state-of-charge) for the cell cycled at 25 °C with IEC profile, already discussed in Section 3.1 and 3.2) at 455 EFC aging.

Regarding the discharge (Fig. 8a), the model provides a consistent simulation in the mid-high SoC part. The effect of C-rate and temperature is properly reproduced. However, the knee and the losses appearing at end of discharge are generally underestimated. This feature might come from different reasons. For instance, large concentration gradients in space (along the jelly roll direction and the through-plane direction) are expected at end of discharge, cumulated over discharge, especially at low temperatures and high C-rate. Second, at low SoC local

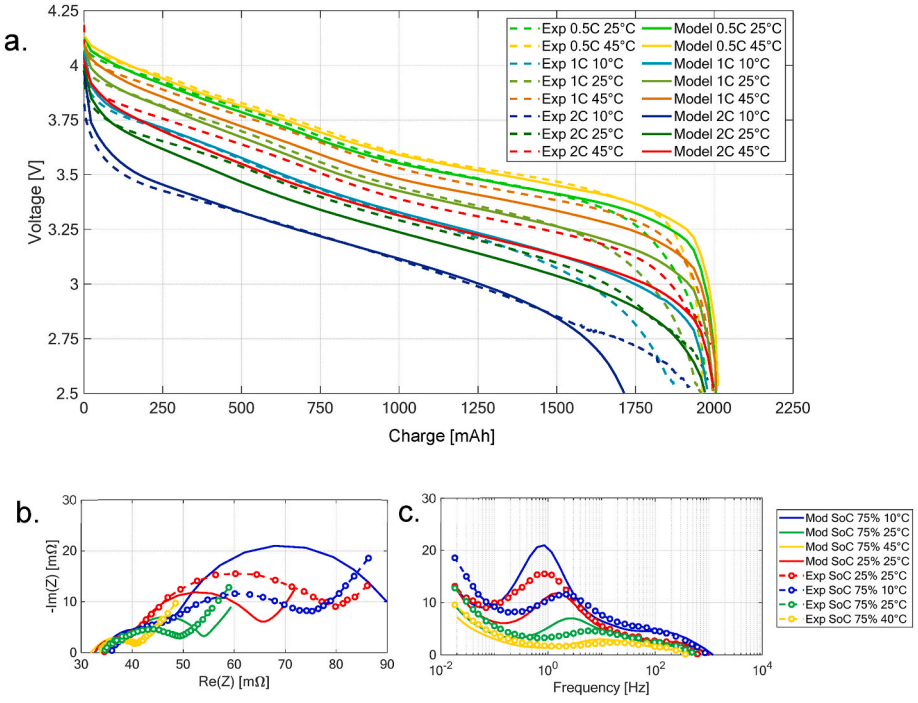

Fig. 8. Simulations of the validation dataset: a) set of discharge and EIS at various operating conditions in b) Nyquist and c) Bode of the imaginary component representations.

heterogeneities in graphite affect the equilibrium potential sensibly. This effect is stressed by low temperature and high C-rate, too. Moreover, slight mis-estimation of electrode balancing could result in larger error at low SoC.

It is worth to remind that this work prioritizes obtaining a general physically-consistent reproduction of performance effects of aging, rather than optimizing the simulation quality for a single, specific operating condition or test. Nevertheless, one possible improvement is the inclusion of a SoC dependence into solid-state lithium diffusivities, which was out of scope for this work. Since the check-up procedure (Section 2.3) includes a high C-rate and low-temperature discharge in the high SoC part, the model provides better results in the first part of the discharge at the expense of a lower accuracy in the low SoC part. As a confirmation, root-mean-square errors are listed in Table 3. The reliability of the simulations is lower with respect to the fresh-cell model [38], but the error becomes much lower if the last portion of the curve is omitted.

Lastly, only some EISs are reported for clarity (Fig. 8b and c). As anticipated, despite the stabilisation of the double layer capacitance, the reaction frequency decreases in the last aging stages, but its detectability was limited by the frequency range of the characterisation procedure (i.e. in Fig. 8, blue curve, the peak occurs for frequencies lower than 1Hz, which is the minimum value that is considered by the optimisation algorithm). The model reproduces the general shape and trends despite being not quantitatively representative. For future works, implementing surface layers in the model and possibly including the activity dependence in the Butler-Volmer formulation of kinetics instead of the linear proportionality with lithium content might improve the reliability and the relation with SoC. Indeed, for instance, V. J. Ovejas et al. [31] observed how overvoltages of graphite show local maxima when the electrode passes from a pure phase to a phase transition, stressing the variability of solid-state diffusivities with lithium concentration.

To summarize, considering the novelty and the complexity in reproducing in a wide range of conditions the physical detrimental effect on performance of an aged cell which underwent complex cycling profile, while ensuring physical consistency between discharge test and EIS, the model-based validation is considered well satisfying.

4.2. Visual inspection after cell opening

Two cells, namely the IEC cycle at 25 °C and 45 °C, are opened in an inert environment at the end of the campaign to perform ex-situ analyses that can verify the interpretation of degradation. First, a visual inspection is carried out. Figure S.11 of the Supplementary Materials reports some scans of the electrodes right after cell opening. The fresh cell properties were already reported in Ref. [18] and they are summarised for clarity.

For both cells, most of the positive electrode coating on the inner side quickly detached from the current collector right during the unrolling of the jelly roll. Only a thin coating layer still adhered to the current collector, which appeared as a matt grey rather than a shiny silver aluminium current collector. This feature has been associated with a mechanical effect in the literature [8]. Pressure lines are evident, especially for the 45 °C cycle, in particular in the areas close to the mandrel. A significant amount of electrode material remained attached on the separator on both sides. Overall, this mechanical brittleness of the positive electrode is related to cycling and pressure lines are a consistent symptom. It is likely that the electrodes had a fragile electrical connection already during operations, and they completely detached as soon as the pressure between adjacent windings was relieved due to cell opening.

Table 3
Root-mean square errors of the simulation of the validation dataset of discharges for the IEC cycle at 25 °C. In bold are highlighted conditions (partially) covered by the calibration dataset. Values in mV. The first column refers to the estimation over the complete discharge, the second neglecting the last 5 % of the curve at low SoC.

Temperature	C-rate					
	0.5C		1C		2C	
10 °C	–	–	85.8	49.9	**51.7**	**25.4**
25 °C	66.9	28.3	**86.1**	**40.3**	52.4	52.3
45 °C	59.3	12.9	46.4	44.9	81.8	83.6

4.3. Validation of LAM with half-cell cycling

The first verification involves the estimation of LAMs, which were investigated in the previous publication [17]. Half-cells of harvested materials are exploited. This method can verify the reliability of the estimation at the time of cell opening, thus at the end of the campaign.

Differential voltage (DV) is chosen because it magnifies the voltage trend while showing capacity variations. Fig. 9 shows the DV plots of both lithiation and delithiation phases of positive (leften sub-figures) and negative (righten sub-figures) electrodes for harvested material from the fresh and the two aged samples. Some half-cells are reported for all the cases. From left to right, voltage decreases (i.e., lithium concentration in the material increases). The analysis of fresh materials has already been reported in Ref. [18]. Here, only the differences between fresh and aged cases are investigated. Shades identify different positions along the roll: light colour for coin cells that were punched close to the mandrel, dark colour for the outer edge. Intermediate intensity is needed for intermediate positions along the role. In Fig. 9e, no pink curve is depicted since the material was very brittle. The exchanged capacity is significantly lower due to the very small amount of active material that remained attached to the current collector. They are considered in relative terms but not for this analysis.

Fig. 9c–e shows the DV of positive electrodes for the IEC cycle at 25 °C and the IEC cycle at 45 °C, respectively. Similarly, Fig. 9d–f refer to the same chart for negative electrodes. For positive electrodes, the shape is preserved, but the amount of exchanged charge is variable. The cell-to-cell variability of exchanged capacity is estimated within 8 % and 26 %, exploiting 6 and 8 coin cells each for the IEC cycle at 25 °C and the IEC cycle at 45 °C, respectively. The datum states that 45 °C cycle is strongly heterogeneous, but no clear pattern is identified regarding the position along the roll, other than the strong material detachment close to the mandrel. Moreover, a decrease with respect to the fresh cells is evident.

Regarding negative electrodes, the shape of aged curves is similar to that of the fresh sample and they show the same hysteresis between lithiation and delithiation phases. The variability of exchanged charge between half-cells of the same original cell is estimated within 7.5 % and 10.9 % over 13 and 13 half-cells each, respectively, for the IEC cycle at 25 °C and at 45 °C. There is a slight general tendency to provide lower performance for cells that were punched close to the mandrel. Overall, the value of capacity is comparable with that of the fresh cell, indicating a narrow level of degradation.

These charts can be scaled to the extractable capacity of the half cell in order to verify the stability of the OCP curve towards ageing, which is a paramount assumption of the equilibrium model that has been exploited for the estimation of LAMs [17]. As in Ref. [18], this verification is achieved for both samples, as reported in Figure S.12 of the Supplementary Materials.

With the same procedure described in Ref. [18], the estimation of LAM can be performed experimentally by quantifying the ratio between specific capacities of aged and fresh half-cells. Specific capacities are reported in Figure S.13 of the Supplementary Materials, as fitting lines over coin-cell capacities. The estimations of LAMs are provided in Table 4. For the results of the algorithm, the extreme of the confidence bands are also present. Interestingly, the estimations of the 45 °C cycle lie within the interval that is identified by the algorithm. On the contrary, the algorithm overestimates the value of LAMn of the 25 °C cycle.

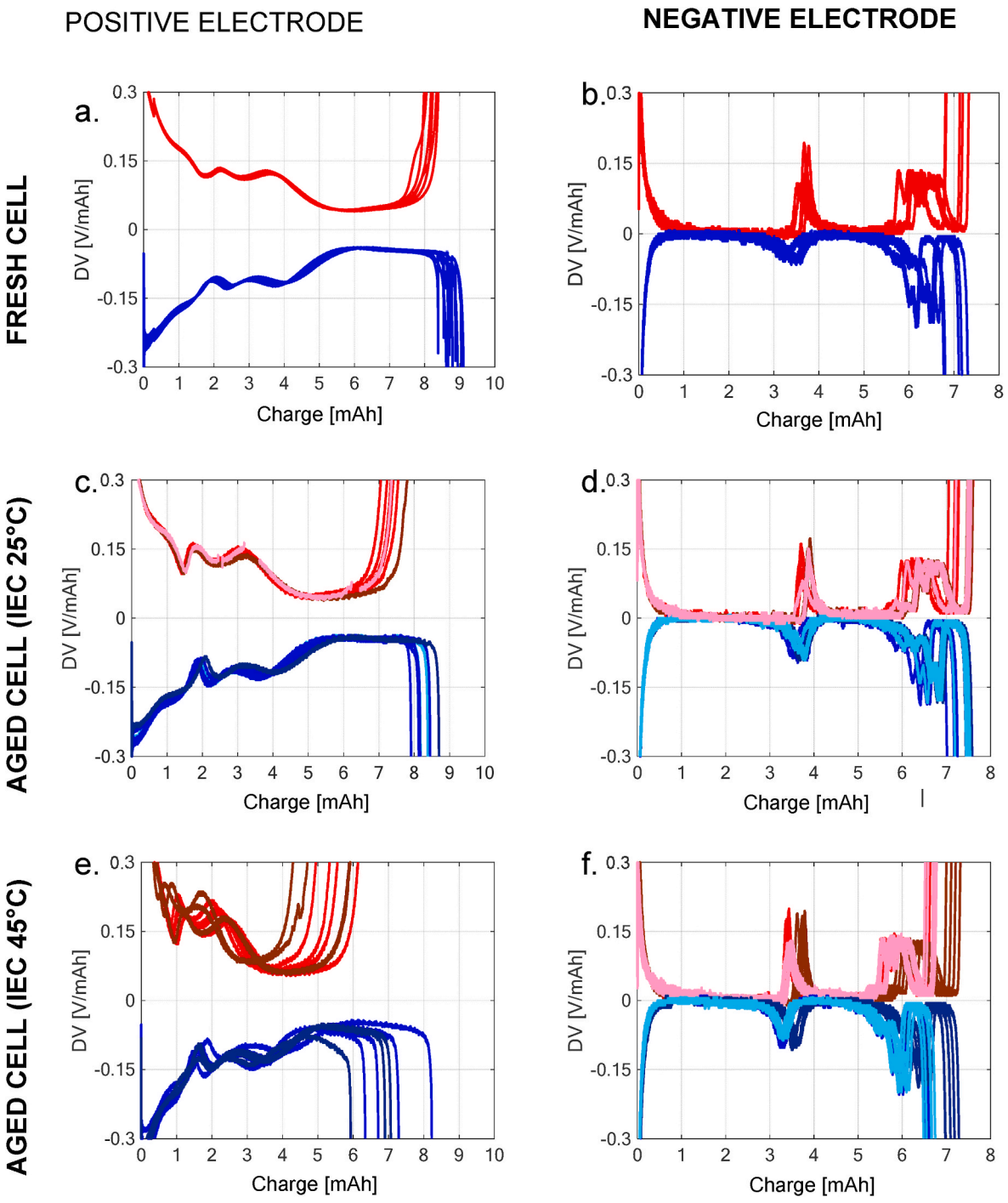

Fig. 9. C/50 lithiation (red curves) and delithiation (blue) DV curves of positive (leften subfigures) and negative (righten subfigures) electrodes of the fresh cell (a–b), IEC cycle at 25 °C (c–d), IEC cycle at 45 °C (e–f), respectively, in half cell configuration.

Table 4
Comparison between the estimation of LAM from half-cell cycling (Exp) and the results of the parameter identification procedure with PSO in terms of optimal value and range.

Cell	Property	Exp	Min	Optimal	Max
IEC cycle at 25 °C	LAMp	8.6 %	8.3 %	11.2 %	12.9 %
	LAMn	2.9 %	5.2 %	7.7 %	10.2 %
IEC cycle at 45 °C	LAMp	21.4 %	17.6 %	19.4 %	21.9 %
	LAMn	10.0 %	7.2 %	9.7 %	12.1 %

Taking into account the accuracy of the experimental datum and possible variations due to the cleaning procedure before coin cell assembly [18], the results are considered satisfactory.

4.4. *Validation of the interpretation through SEM and EDS*

Morphology and chemical composition are investigated here through SEM and EDS, respectively. Negative electrodes are first compared with the fresh sample, described in Ref. [11] and reported here to ease the comparisons.

4.4.1. Negative electrode

SEM of the negative electrode of IEC 25 °C is depicted in Fig. 10c and d, while the corresponding images of the fresh material are shown in Fig. 10a and b. No strong variation in particle size and shape is detected. Nevertheless, Fig. 10d shows a large exfoliation of graphite with respect to the fresh sample. Even though the image is restricted to a small area, the occurrence of this characteristic is quite widespread in the SEM sample. Exfoliation can explain the trend of LAMn, suggesting the utilization of a lower amount of active sites. Moreover, exfoliation provides a fresh surface in contact with the electrolyte, thus enhancing SEI growth and the associated lithium loss. Differently from the calendar-aged sample that was investigated in Ref. [18], SEI is not observed, which can be related to the mechanical stresses induced by cycling that broke it down. SEI growth is likely to have taken place, but it has not created a uniform covering layer.

However, by investigating the chemical composition (Table 5), a larger oxygen and fluorine content is detected with respect to the fresh sample. This is consistent with electrolyte degradation, forming SEI [6, 39].

SEM images of the cell that has been cycled at 45 °C are reported in Fig. 10Fig. 10e-f. Again, no strong variation in particle size and shape is evident. However, the figure looks blurred, and white spots are present. With a large magnification (Fig. 10f), the nature of particles is revealed as significantly affected by exfoliation. Also, this feature is quite widespread in this sample and may reflect the whitish appearance of Fig. 10e. Chemical analyses are similar to the cycle at 25 °C, with the growth of oxygen and fluorine contents, which suggest the development of SEI due to electrolyte degradation. White spots in Fig. 10e show the composition of the positive electrode, but they are neglected since the contamination of the samples might have occurred.

4.4.2. Positive electrode

The same analysis is conducted for the positive electrode materials. The 1000x magnified image of the cycle at 25 °C (Fig. 11c) resembles that of the fresh material (Fig. 11a). In the zoomed view (Fig. 11d), some cracks are identified in the secondary particles (one is highlighted with a red circle), which may reflect the mechanical stresses due to cycling. No evidence of surface layers is present. Unfortunately, the chemical analysis is not available.

Also, for the cycle at 45 °C, no sign of degradation on a large scale is detected (Fig. 11e). However, it is very clear how some particle cracking has occurred in Fig. 11f. Its occurrence is seldom in the investigated sample, but a larger spread is expected inside the coating thickness. It supports the role of cycling and depth of discharge in triggering a mechanical degradation of the electrode at the micron scale. Lastly, no sign of strong transition metal dissolution is recorded since the chemical composition is similar to that of the fresh electrode (Table 6). No considerations regarding CEI growth can be made.

4.5. Final remarks of the validation activity

First, simulations of validation conditions of the aged sample are in qualitative agreement with the experiments, though possible improvements can increase the quantitative consistency. Overall, the modelling tool provides satisfactory results, considering the relatively wide range of conditions and the aged state.

The interpretation of degradation is then verified through different techniques to validate the suitability of the diagnostic methodology in identifying the degradation phenomena according to the evolution of physical parameters. First, the cycling of half-cells with harvested material enables the estimate of the LAM value at the end of the campaign by estimating the specific capacity of the aged material. Considering the uncertainty of the experimental measurements and the modelling analyses, the experimental value is close enough to the model value, supporting the results of thermodynamic analysis.

Lastly, morphological and chemical analyses are reported. Cycled

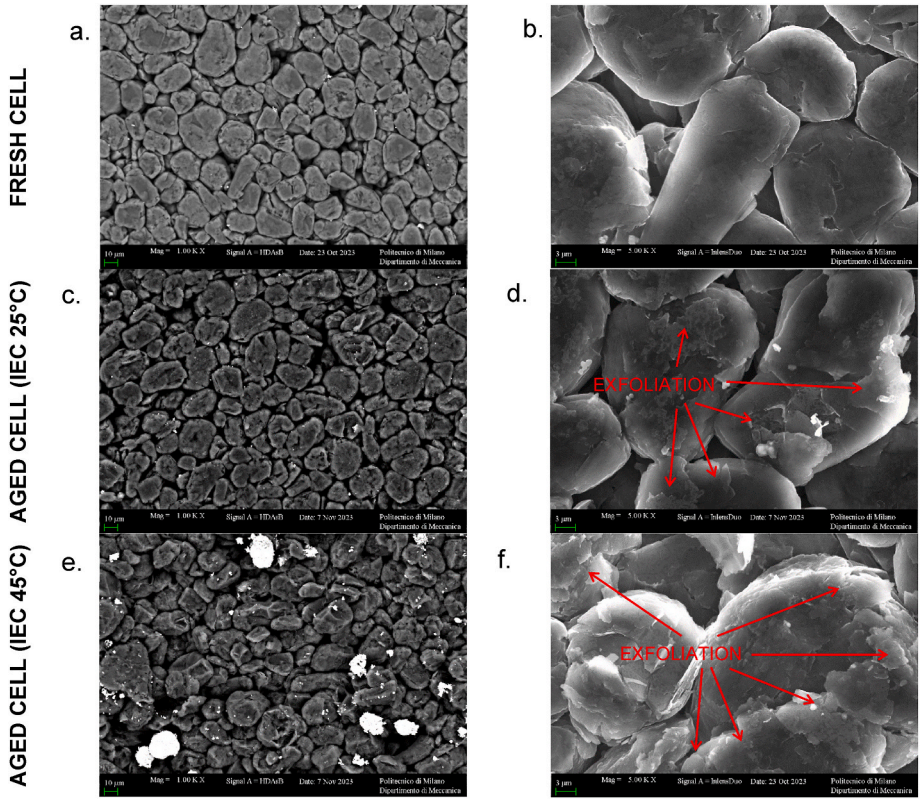

Fig. 10. SEM images of fresh and aged electrodes at 1000x (leften subfigures) and 5000x (righten) magnifications. Lens type in the legend under the subfigures. Fresh (subfigures a-b), cycle at 25 °C (c–d) and cycle at 45 °C (e–f).

Table 5
Chemical composition by atomic mass of negative electrodes. If not specified, quantities are averages over ~1 mm^2 areas.

Original cells	Element atomic fraction in negative electrode [%]								
	C	O	F	Al	P	Mn	Co	Ni	Cu
Fresh	91.12	5.65	2.67	0	0.35	0	0	0	0.16
Cycle 25 °C	83.07	12.05	4.11	0	0.52	0.02	0	0	0.2
Cycle 45 °C	81.1	13.4	4.79	0	0.5	0.03	0	0	0.2

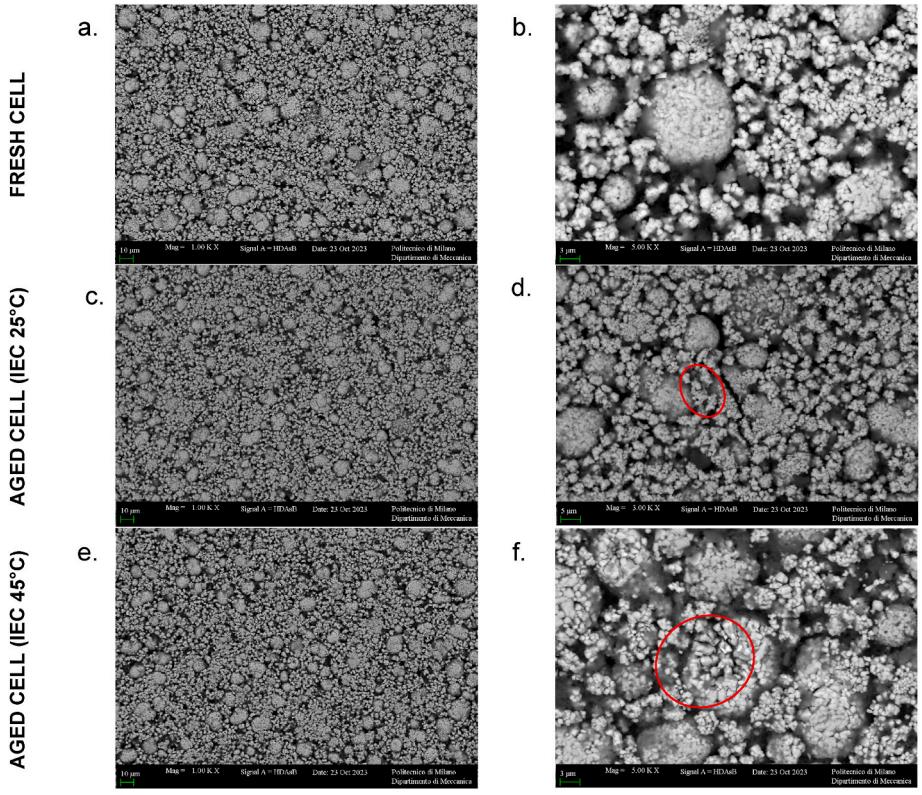

Fig. 11. SEM images of fresh and aged electrodes at 1000x (leften subfigures) and 5000x (righten) magnifications. Lens type in the legend under the subfigures. Fresh (subfigures a-b), cycle at 25 °C (c–d) and cycle at 45 °C (e–f).

Table 6
Chemical composition by atomic mass of positive electrodes. Quantities are averages over ~1 mm^2 areas.

Original cells	Element atomic fraction in positive electrode [%]								
	C	O	F	Al	P	Mn	Co	Ni	Cu
Fresh	42.04	31.43	14.27	0.12	0.33	4.45	2.1	5.26	0
Cycle 45 °C	42.1	29.6	15	0.1	0.4	4.81	2.28	5.6	0

positive electrodes appear brittle at the macro scale, showing particle cracking on the micron scale. Both observations agree with the mechanical origin of active electrode loss. Differently, cycled graphites are exfoliated, which might justify the value of LAMn, and the increase of oxygen and fluorine content supports that SEI growth has taken place.

5. Conclusions

This work investigated the degradation of commercial lithium-ion batteries under realistic conditions and highly dynamic loads, typical of automotive application, exploiting a physical model.

Performance decay is traced with periodic non-invasive check-up procedures, combining partial discharges and EIS measurements, exploited to perform the parameter identification of P2D physical models. In this way, we demonstrate a physical-based interpretation of aging which goes beyond the quantification of capacity fade and resistance increase, on which state-of-health is typically based. The method is applied on the distinction of the aging effects of different meaningful operating conditions, close to automotive application, paving the way for physics-informed prognostic methods.

The following are the most important outcomes:

- Electrolyte decay is identified to be one of the main responsible of resistance increase. Its conductivity loss is found to decrease strongly and linearly over cycles, possibly due to gas release or SEI growth, and looks correlated with LLI mechanism and consistently increased by operating temperature.
- The positive electrode is also crucially impacting battery durability. It is identified to be affected by particle cracking proportional to number of cycles and with DoD. Also, significant diffusion

limitations and worsening of the kinetics of the reaction are identified, whose effects are yet hard to be deconvolved without dedicated investigations. However, this approach can advance the discussion on these topics in the scientific community, especially regarding diffusive limitations.
- Apart from being detrimental for battery performance, P2D simulations reveal that the reduction of electrolyte conductivity and solid-state diffusivity in positive electrodes is responsible for progressively heterogeneous operation of the aged cells.
- Interestingly, no effect is detected due to different charging C-rates, while the IEC profile induces a similar degradation with respect to the WLTP load, apart from a faster electrolyte consumption, which might be related to the high C-rates. IEC 62660-1 seems an interesting solution for laboratory testing, providing a realistic degradation with respect to a real application while saving testing time.

The results have been verified with additional measurements and post-mortem analyses. In particular,

- The identification of thermodynamic parameters agrees with the estimations from half-cell cycling, confirming loss of active material especially at positive electrode. Occurrence of particle cracking, most likely leading to such LAM, is confirmed with SEM on cycled cells, supporting the interpretation of the DoD effect.
- Electrochemical testing on half-cells also confirms that modifications of the impedance spectra are associated with the positive electrode.
- Variations of the chemical composition of the positive electrodes are few, suggesting that if any chemical mechanism like transition metal dissolution or cation mixing has occurred, its extent is limited.

Overall, the methodology proved its strength in interpreting degradation and its reliability against verification measurements. It is a step forward both from a methodological perspective, providing a robust physics-based approach strategy to consolidate degradation studies, and also from an application perspective, proposing a widely-applicable diagnostic tool and relating real-world operating conditions with specific degradation mechanisms and the involved components.

CRediT authorship contribution statement

G. Sordi: Writing – review & editing, Writing – original draft, Visualization, Validation, Methodology, Investigation, Formal analysis, Data curation, Conceptualization. **A. Stecchini:** Visualization, Investigation, Formal analysis, Conceptualization. **R. Evangelista:** Visualization, Investigation, Formal analysis, Conceptualization. **D. Luder:** Writing – review & editing, Investigation. **W. Li:** Writing – review & editing, Supervision. **D.U. Sauer:** Supervision. **A. Casalegno:** Writing – review & editing, Supervision, Project administration, Funding acquisition. **C. Rabissi:** Writing – review & editing, Supervision, Project administration, Funding acquisition, Conceptualization.

Declaration of competing interest

The authors declare that they have no known competing financial interests or personal relationships that could have appeared to influence the work reported in this paper.

Acknowledgements

This work was supported by the European Union's Horizon 2020 Research and Innovation Program [Grant Agreement No. 873111, project "DigiPrime - Digital Platform for Circular Economy in Cross-sectorial Sustainable Value Networks"] and the Energy for Motion initiative of Politecnico di Milano as part of Energy department recognition as Department of Excellence 2018–2020 from Italian Ministry of Education, Universities and Research (MIUR).

The authors would like to acknowledge Andrea Rondi and Davide Conti for their support in the experimental campaign at 45 °C and early simulations and Ludovica Rovatti and Rasheed Michael Ishola for their help in performing SEM analysis. Moreover, G.S. would like to acknowledge the IDEA League for funding his research exchange at RWTH Aachen University, Germany.

Appendix A. Supplementary data

Supplementary data to this article can be found online at https://doi.org/10.1016/j.etran.2025.100410.

List of acronyms

Acronym	Description
BOL	Begin of life
CEI	Cathode Electrolyte Interphase
DoD	Depth of Discharge
DV	Differential Voltage
EDS	Energy Dispersive X-ray Spectroscopy
EFC	Equivalent Full Cycles
EIS	Electrochemical Impedance Spectroscopy
HFR	High-Frequency Resistance
IEC	International Electrotechnical Commission
LAM	Loss of Active electrode Material
LIB	Lithium-ion Battery
LLI	Loss of Lithium Inventory
LMO	Lithium-manganese-oxide battery
NCA	Lithium-nickel-cobalt-aluminum-oxide battery
NMC	Lithium-nickel-manganese-cobalt-oxide battery
OCP	Open-Circuit Potential
P2D	Pseudo-two Dimensional model
PSO	Particle Swarm Optimisation
SEI	Solid Electrolyte Interphase
SEM	Scanning Electron Microscope
SoC	State of Charge
WLTP	Worldwide harmonised Light vehicles Test Procedure

Data availability

Data will be made available on request.

References

[1] Edge JS, O'Kane S, Prosser R, Kirkaldy ND, Patel AN, Hales A, Ghosh A, Ai W, Chen J, Yang J, Li S, Pang MC, Bravo Diaz L, Tomaszewska A, Marzook MW, Radhakrishnan KN, Wang H, Patel Y, Wu B, Offer GJ. Lithium ion battery degradation: what you need to know. Phys Chem Chem Phys 2021;23:8200–21. https://doi.org/10.1039/d1cp00359c.

[2] Barré A, Deguilhem B, Grolleau S, Gérard M, Suard F, Riu D. A review on lithium-ion battery ageing mechanisms and estimations for automotive applications. J Power Sources 2013;241:680–9. https://doi.org/10.1016/j.jpowsour.2013.05.040.

[3] Guo J, Li Y, Pedersen K, Stroe DI. Lithium-ion battery operation, degradation, and aging mechanism in electric vehicles: an overview. Energies (Basel) 2021;14. https://doi.org/10.3390/en14175220.

[4] Wang J, Purewal J, Liu P, Hicks-Garner J, Soukazian S, Sherman E, Sorenson A, Vu L, Tataria H, Verbrugge MW. Degradation of lithium ion batteries employing graphite negatives and nickel-cobalt-manganese oxide + spinel manganese oxide positives: Part 1, aging mechanisms and life estimation. J Power Sources 2014;269:937–48. https://doi.org/10.1016/j.jpowsour.2014.07.030.

[5] Keil P, Jossen A. Impact of dynamic driving loads and regenerative braking on the aging of lithium-ion batteries in electric vehicles. J Electrochem Soc 2017;164:A3081–92. https://doi.org/10.1149/2.0801713jes.

[6] Maheshwari A, Heck M, Santarelli M. Cycle aging studies of lithium nickel manganese cobalt oxide-based batteries using electrochemical impedance spectroscopy. Electrochim Acta 2018;273:335–48. https://doi.org/10.1016/j.electacta.2018.04.045.

[7] Luo G, Zhang Y, Tang A. Capacity degradation and aging mechanisms evolution of lithium-ion batteries under different operation conditions. Energies (Basel) 2023;16. https://doi.org/10.3390/en16104232.

[8] Jalkanen K, Karppinen J, Skogström L, Laurila T, Nisula M, Vuorilehto K. Cycle aging of commercial NMC/graphite pouch cells at different temperatures. Appl Energy 2015;154:160–72. https://doi.org/10.1016/j.apenergy.2015.04.110.

[9] Uddin K, Perera S, Widanage WD, Somerville L, Marco J. Characterising lithium-ion battery degradation through the identification and tracking of electrochemical battery model parameters. Batteries 2016;2. https://doi.org/10.3390/batteries2020013.

[10] Ramadesigan V, Chen K, Burns NA, Boovaragavan V, Braatz RD, Subramanian VR. Parameter estimation and capacity fade analysis of lithium-ion batteries using reformulated models. J Electrochem Soc 2011;158:A1048. https://doi.org/10.1149/1.3609926.

[11] Zhang L, Wang L, Lyu C, Li J, Zheng J. Non-destructive analysis of degradation mechanisms in cycle-aged graphite/LiCoO2 batteries. Energies (Basel) 2014;7:6282–305. https://doi.org/10.3390/en7106282.

[12] Kim J, Chun H, Kim M, Han S, Lee JW, Lee TK. Effective and practical parameters of electrochemical Li-ion battery models for degradation diagnosis. J Energy Storage 2021;42. https://doi.org/10.1016/j.est.2021.103077.

[13] Lin WJ, Chen KC. Evolution of parameters in the Doyle-Fuller-Newman model of cycling lithium ion batteries by multi-objective optimization. Appl Energy 2022;314. https://doi.org/10.1016/j.apenergy.2022.118925.

[14] Lyu C, Song Y, Zheng J, Luo W, Hinds G, Li J, Wang L. In situ monitoring of lithium-ion battery degradation using an electrochemical model. Appl Energy 2019;250:685–96. https://doi.org/10.1016/j.apenergy.2019.05.038.

[15] Li J, Wang D, Deng L, Cui Z, Lyu C, Wang L, Pecht M. Aging modes analysis and physical parameter identification based on a simplified electrochemical model for lithium-ion batteries. J Energy Storage 2020;31. https://doi.org/10.1016/j.est.2020.101538.

[16] Fan G, Lu D, Trimboli MS, Plett GL, Zhu C, Zhang X. Nondestructive diagnostics and quantification of battery aging under different degradation paths. J Power Sources 2023;557. https://doi.org/10.1016/j.jpowsour.2022.232555.

[17] Sordi G, Rondi A, Conti D, Casalegno A, Rabissi C. Degradation of lithium-ion batteries under automotive-like conditions: aging tests, capacity loss and q-OCP interpretation. Future Batteries 2024;3:100005. https://doi.org/10.1016/j.fub.2024.100005.

[18] Sordi G, Luder D, Li W, Sauer DU, Casalegno A, Rabissi C. Investigation of calendar ageing of lithium-ion battery through physical models with ex-situ validation. J Power Sources 2024;615:235076. https://doi.org/10.1016/j.jpowsour.2024.235076.

[19] Sordi G, Sedzik M, Casalegno A, Rabissi C. Diagnosis of lithium-ion batteries degradation with P2D model parameters identification: a case study on low temperature charging. Future Batteries 2024:100006. https://doi.org/10.1016/j.fub.2024.100006.

[20] Sony Energy Devices Corporation. Lithium ion rechargeable battery technical information model US18650V3. 2011.

[21] British Standard Institution. Secondary lithium-ion cells for the propulsion of electric road vehicles. 2019.

[22] Rabissi C, Sordi G, Innocenti A, Casalegno A. Fast and reliable calibration of thermal-physical model of lithium-ion battery: a sensitivity-based method. J Energy Storage 2023;59. https://doi.org/10.1016/j.est.2022.106435.

[23] Yang X, Chen L, Xu X, Wang W, Xu Q, Lin Y, Zhou Z. Parameter identification of electrochemical model for vehicular lithium-ion battery based on particle swarm optimization. Energies (Basel) 2017;10. https://doi.org/10.3390/en10111811.

[24] Shafiei Sabet P, Warnecke AJ, Meier F, Witzenhausen H, Martinez-Laserna E, Sauer DU. Non-invasive yet separate investigation of anode/cathode degradation of lithium-ion batteries (nickel–cobalt–manganese vs. graphite) due to accelerated aging. J Power Sources 2020;449. https://doi.org/10.1016/j.jpowsour.2019.227369.

[25] Ovejas VJ, Cuadras A. Impedance characterization of an LCO-NMC/graphite cell: ohmic conduction, sei transport and charge-transfer phenomenon. Batteries 2018;4. https://doi.org/10.3390/batteries4030043.

[26] Stiaszny B, Ziegler JC, Krauß EE, Schmidt JP, Ivers-Tiffée E. Electrochemical characterization and post-mortem analysis of aged LiMn 2O4-Li(Ni0.5Mn0.3Co 0.2)O2/graphite lithium ion batteries. Part I: cycle aging. J Power Sources 2014;251:439–50. https://doi.org/10.1016/j.jpowsour.2013.11.080.

[27] Galushkin NE, Yazvinskaya NN, Galushkin DN. Mechanism of gases generation during lithium-ion batteries cycling. J Electrochem Soc 2019;166:A897–908. https://doi.org/10.1149/2.0041906jes.

[28] Strauss F, Teo JH, Schiele A, Bartsch T, Hatsukade T, Hartmann P, Janek J, Brezesinski T. Gas evolution in lithium-ion batteries: solid versus liquid electrolyte. ACS Appl Mater Interfaces 2020;12:20462–8. https://doi.org/10.1021/acsami.0c02872.

[29] Zhou X, Huang J, Pan Z, Ouyang M. Impedance characterization of lithium-ion batteries aging under high-temperature cycling: importance of electrolyte-phase diffusion. J Power Sources 2019;426:216–22. https://doi.org/10.1016/j.jpowsour.2019.04.040.

[30] Stiaszny B, Ziegler JC, Krauß EE, Zhang M, Schmidt JP, Ivers-Tiffée E. Electrochemical characterization and post-mortem analysis of aged LiMn 2O4-NMC/graphite lithium ion batteries part II: calendar aging. J Power Sources 2014;258:61–75. https://doi.org/10.1016/j.jpowsour.2014.02.019.

[31] Ovejas VJ, Cuadras A. State of charge dependency of the overvoltage generated in commercial Li-ion cells. J Power Sources 2019;418:176–85. https://doi.org/10.1016/j.jpowsour.2019.02.046.

[32] Liu G, Zheng H, Song X, Battaglia VS. Particles and polymer binder interaction: a controlling factor in lithium-ion electrode performance. J Electrochem Soc 2012;159:A214–21. https://doi.org/10.1149/2.024203jes.

[33] Foster JM, Huang X, Jiang M, Chapman SJ, Protas B, Richardson G. Causes of binder damage in porous battery electrodes and strategies to prevent it. J Power Sources 2017;350:140–51. https://doi.org/10.1016/j.jpowsour.2017.03.035.

[34] Liu H, Foster JM, Gully A, Krachkovskiy S, Jiang M, Wu Y, Yang X, Protas B, Goward GR, Botton GA. Three-dimensional investigation of cycling-induced microstructural changes in lithium-ion battery cathodes using focused ion beam/scanning electron microscopy. J Power Sources 2016;306:300–8. https://doi.org/10.1016/j.jpowsour.2015.11.108.

[35] Schuster SF, Bach T, Fleder E, Müller J, Brand M, Sextl G, Jossen A. Nonlinear aging characteristics of lithium-ion cells under different operational conditions. J Energy Storage 2015;1:44–53. https://doi.org/10.1016/j.est.2015.05.003.

[36] Raj T, Wang AA, Monroe CW, Howey DA. Investigation of path-dependent degradation in lithium-ion batteries. Batter Supercaps 2020;3:1377–85. https://doi.org/10.5287/bodleian:v0ervBv6p.

[37] Baure G, Dubarry M. Synthetic vs. Real driving cycles: a comparison of electric vehicle battery degradation. Batteries 2019;5. https://doi.org/10.3390/batteries5020042.

[38] Sordi G, Rabissi C, Casalegno A. Reliable thermal-physical modeling of lithium-ion batteries: consistency between high-frequency impedance and ion transport. Energies (Basel) 2023;16. https://doi.org/10.3390/en16124730.

[39] Zhu W, Zhou P, Ren D, Yang M, Rui X, Jin C, Shen T, Han X, Zheng Y, Lu L, Ouyang M. A mechanistic calendar aging model of lithium-ion battery considering solid electrolyte interface growth. Int J Energy Res 2022;46:15521–34. https://doi.org/10.1002/er.8249.